Honours Project Thesis

Modeling the Geometry of the Quark Gluon Plasma

Ben Bert

Supervisor
A. Prof. W.A. Horowitz

Co-Supervisor
Cole Faraday

Abstract

We introduce and extend upon a model, known as the Djordjevic-Gyulassy-Levai-Vitev (DGLV) model, which describes the energy dissipation of jets traversing the quark gluon plasma (QGP), a phenomenon observed following high-energy particle collisions in accelerators such as the Large Hadron Collider (LHC) and the Relativistic Heavy Ion Collider (RHIC). The model is derived from perturbative quantum chromodynamics (pQCD) and as such leads to exceedingly complex analytics. This project highlights the challenges of extracting predictions from pQCD that can be observed at the LHC and RHIC. The particular challenge we aim to overcome is to find a simplification of the QGP's geometry which still yields accurate results; this simplification is necessary to yield quantitative results that are comparable to experimental data. More precisely, we wish to perform a calculation that captures the hydrodynamic and geometric characteristics of the QGP; while still under the simplifying assumption that allows our numerical models to converge in a finite amount of time. Our results show that the energy loss is sensitive to the geometric assumptions of the structure of the QGP, where slight modifications to the geometry led to noticeable variations in the results.

Acknowledgements

Firstly, I would like to thank Prof. Horowitz for his dedication to ensuring that all his students have a platform to express all their ideas and opinions in a way that feels safe and natural. From day one, Prof. Horowitz has provided me with guidance in terms of career choices, but he has also guided me in finding what it is exactly that I do and do not enjoy in physics. I would like to thank him especially for all the Friday lunches that he organized with the rest of his research team.

Then to Cole, who I would like to thank for not only helping me understand many of the finer and more technical details that came along with this project, but even more so I would like to thank Cole for helping me find the many (and boy do I mean *many*) bugs that I encountered in the numerical aspects of this project.

I would also like to thank my grandparents, Gramps and Gran, for the obvious financial support they provided me with; but beyond that I would like to thank them for giving me the confidence to actually pack up my bags and come down to Cape Town all on my own and complete an honours degree!

Lastly, I would like to thank my mother Gaëlle and sibling Jo for all the emotional support they provided. This year was stressful and filled with much self-doubt, but with Gaëlle and Jo provided me with a calming escape from it all.

Oh, and of course, thanks to the rest of the physics honours class for descending into utter madness with me

Contents

1

Introduction

Doing research in physics requires many little creative increments of advancement. These increments may at times feel well motivated by what came before (and on occasion, they may even be logically sound). However, the ultimate judgement of the validity of the increments comes from their agreement with experimental fact. Nature has an amusing, and perhaps sadistic, approach to letting the physicist know when they have strayed off course. This project is just one example of such an occurrence. The ultimate goal of this project, is to understand through a theoretical approach some of the recent experimental observables that have been found at Relativistic Heavy Ion Collider (RHIC) and the Large Hadron Collider (LHC). RHIC and the LHC are two high energy particle colliders testing the frontiers of the Standard Model. The LHC and RHIC collide heavy atoms (such as gold and lead) to generate a plasma that is formed at extremely high temperatures (comparable to the temperatures of the early universe). The plasma is known as the quark gluon plasma (QGP). Guided and motivated by the results at RHIC and the LHC, many theoretical energy loss models have been developed to describe the phenomenological characterises of patrons (quarks or gluons) as they move through the QGP [1, 2]. In this project we shall work with the Djordjevic-Gyulassy-Levai-Vitev (DGLV) energy loss model [3], with the ambition to further improve on its capabilities in describing the properties of the QGP.

This manuscript will serve two purposes. The first will be to succinctly describe the features of the model, and this will be aimed at non-experts in this specific sub-field of phenomenological particle physics. The second purpose of this manuscript will be to provide a source for future work where many of the minutia of the details of the model can be found and easily referenced.

1.1 From QCD to the QGP

The interactions within the QGP are governed by the strong nuclear force, which is described by the theory known as quantum chromodynamics (QCD). The seeds of QCD can be traced back to as far as Rutherford's scattering experiments in 1911. Rutherford had pointed out that there must exist some mechanism in which the protons within the nucleus – which are all positively charged – attract each other and in turn keep the nucleus of the atom stable [4]. It wasn't until 1934 that a model of the strong force was presented. The model presented by Yukawa introduced an exchange force via a virtual boson [5]. Following Yukawa and the advent of quantum field theory (QFT), the interactions between particles became to be understood as the exchange between force carrying particles [6]. The first example of this particle-force duality arose in quantum electrodynamics (QED) where the forces carried by the electromagnetic field were to be described as the exchange of photons between interacting bodies. This analogy was then extended to give rise to the boson particles which acted as the force carriers of the weak (W and Z bosons) and strong force (gluons). The weak interactions of the heavy W and Z bosons were accredited as the responsible interaction for the well studied beta decay processes. While the massless gluons mediated the strong force and hence, were responsible for keeping the nucleus stable — ultimately providing an answer to Rutherford's postulated mechanism.

Experimentally, physicists were discovering a plethora of new particles (generically known as hadrons) and the term "*The Particle Zoo*" was coined to describe the state of physics at this time. The proliferation of newly discovered particles started with Anderson and Neddermeyer in 1937 as they studied the energy loss of particles originating from cosmic ray showers [7]. Gell-Munn and independently Ne'eman developed the *Eightfold Way* – a classification scheme to organize and understand the proliferation of the new particles [8, 9]. Pushing on from the *Eightfold Way*, Gell-Munn along with Zweig proposed an underlying substructure – based off the SU(3) symmetry group – that described the new collection of particles as a composition of more fundamental constituents of matter [10, 11]. This new constituent matter – named as the *Quark* by Gell-Munn – could be combined in different configurations, these different configurations could then give rise to the observed particles of *The Particle Zoo*.

In rudimentary terms, the quarks are held together by the gluons, the mediators of the strong force. The gluons are particles that are color charged. Color charge is similar to the electric charge, but instead it has three flavours, namely: red, green and blue. A combination of red, green and blue charge would result in a neutral (white) color charge. Unlike photons, gluons can interact with each other. This makes QCD an inherently more complicated theory than that of QED. At low energies the interactions between gluons and quarks are strongly coupled leading to confinement of the quark-gluon composite state into hadronic forms of matter. At these low energy scales perturbative techniques cannot be used to describe QCD and the mechanism for explaining confinement is one of the most outstanding problems in physics [12]. It was originally thought that the quarks and gluons could not exist individually and be unbounded from each other. But circa 1973 Gross, Wilczek and independently Politzer discovered that at higher energies the interactions become more weakly coupled giving rise to asymptotic freedom (see fig. 1), which in turn, allowed for the the quark interactions to be studied perturbatively [13, 14]. The asymptotic freedom gives rise to the process of deconfinement of hadrons and it is in this deconfined state of quarks and gluons that a plasma forms — the plasma is known as the QGP.

The QGP offers a rich ground for exploring the principles of QCD, as the dynamics of the QGP are fundamentally linked to the behaviours of quarks and gluons. Furthermore, the QGP offers a unique window into the high temperature state of the early universe. By replicating these extreme conditions of the early universe, physicists can investigate the phase transitions (fig. 2), hadron formation that occurred during its initial stages. Thus, research on the QGP not only elucidates the behavior of quarks and gluons but also provides valuable insights into the fundamental processes that shaped the universe's early history.

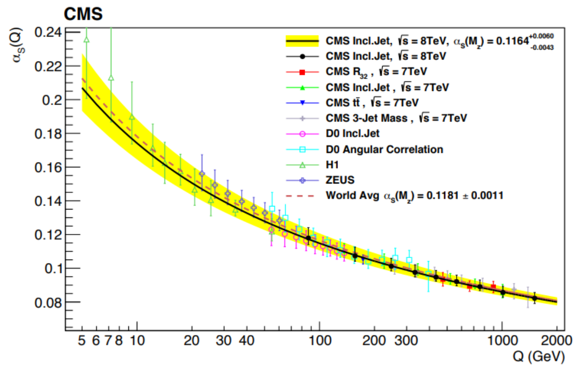

Figure 1: Coupling (α_s) as a function of the energy scale (Q). As the energy scale is increased α_s, which determines the strength of the coupling between the quarks and gluons decreases [15]. The decrease in the coupling strength at high energies results in deconfinement of the quarks and gluons from bound states and allows the partons to become free from one another; this process is known as asymptotic freedom.

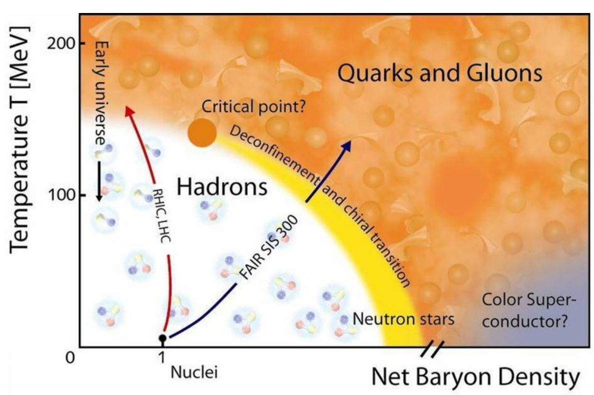

Figure 2: Phase diagram of the QGP with baryon density on the horizontal axis and temperature on the vertical axis (baryons are colour neutral, three-quark bound states) [16]. At the particle accelerators of RHIC and the LHC, temperature scales are believed to be extreme enough for the relevant degrees of freedom to describe matter to be that of the quarks and gluons; at more moderate temperature scales the relevant degrees of freedom are those of the baryons.

1.2 Probing the QGP

Soon after the Big Bang ($< 20\mu s$), the universe was exclusively filled with the QGP as temperatures were initially too high for hadronization to take place [17]. The particle accelerators at RHIC and the LHC are able to recreate these extreme conditions by colliding heavy atomic matter at ultra high energy scales in so called *AA collisions*. This allows one to study the QGP that forms (albeit very briefly, as the QGP only lasts in these collisions for time scales on the order of $\sim 10^{-22}s$ [18]) as a result of the impact between the colliding particles.

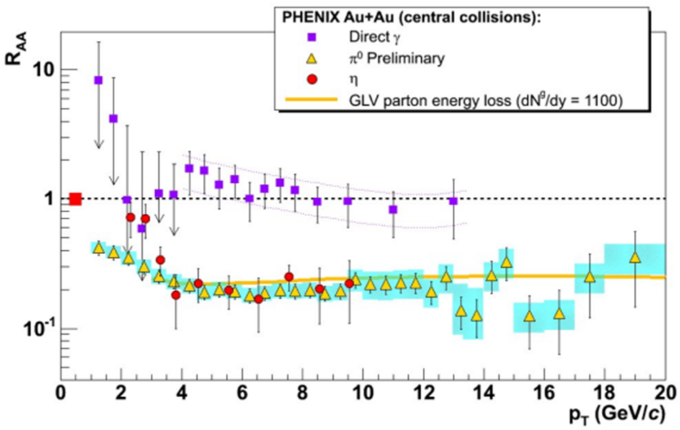

Figure 3: R_{AA} as a function of p_T [19, 20]. The R_{AA} is an indication of the energy loss that occurs in the QGP (see section 2 for more details). Jet quenching occurs at the parton level rather than the hadron level for high p_T collisions. This means that the suppression is driven solely by the energy lost by the parent quark or gluon in the quark-gluon plasma (QGP) medium, and not by the final observed hadron. This is evident from the similar levels of suppression observed in light hadrons such as the π^0 and η particles, despite their differing masses.

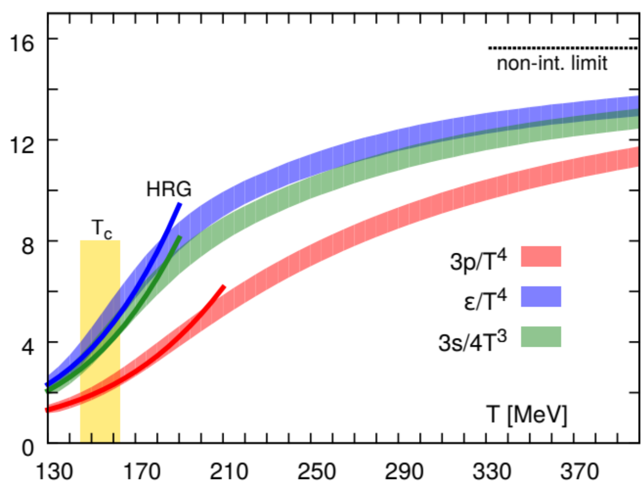

Figure 4: Pressure and energy density normalized to the fourth power of the temperature T with the entropy density normalized to the third power of the temperature. The solid lines are the prediction of the Hadron Resonance Gas model while the opaque bands are the Lattice QCD calculations of the HotQCD Collaboration [21, 22]. At the critical temperature of $T_c \approx 150$MeV, the results for the hadron gas begin to differ qualitatively from the Lattice predictions, suggesting that the hadrons are no longer the correct degrees of freedom to describe the system for temperatures beyond T_c

Following a collision, particles carrying color charge can fragment from the original composite particle involved in the collision. But these color charged particles interact with the QGP and lose energy and, as a result, combine with other color charged particles to become re-confined into a composite state. The composite states (hadrons) of color charged particles tend to all travel in the same direction and forming at *jet* of many hadrons — the jets then interact with the QGP and dissipate their energy to the medium (this phenomenon is termed as *jet quenching*). The jet quenching is primarily due to the energy loss that occurs on the partonic scale [23].

2

Nuclear Modification Factor

The actual energy loss of the particles within the jets are not experimentally accessible. However, there are other (more statistical) methods for understanding how the particles, and in particular, how the partons within the jets lose energy. One method is by measuring the nuclear modification factor (or, as is common the literature, the R_{AA}) of outgoing hadrons as a function of p_T; the R_{AA} is defined as [24]:

$$R_{AA} := \frac{dN_{AA}/dp_T}{N_{coll}\, dN_{pp}/dp_T} \tag{1}$$

where N_{AA} is the number of leading hadrons detected in a heavy ion collision, N_{pp} is the number of hadrons detected in a proton-proton collision and N_{coll} is the total number of binary nucleon-nucleon collisions . The nuclear modification factor is a rough measure of the energy loss of the partons moving through the QGP. The normalization term of N_{coll} in the definition of the R_{AA} can be thought of as the number of proton-proton-like collisions in a AA collision. If one then assumes that any suppression observed in the spectra of an AA collision is due to the QGP and that no QGP forms during a proton-proton collision; then one can interpret an $R_{AA} \sim 1$ as a collision in which no QGP formed and thus no energy loss occurring, conversely an $R_{AA} < 1$ suggests that the QGP has formed and thus energy loss has taken place.

Integral Form of the R_{AA}

The definition of the R_{AA} in eq. (1) does not lead to theoretically tractable results. Following the work done by Horowitz [24] we can find an approximate form of eq. (1) by considering the case of a parton losing fractional energy loss x during an event.

$$R_{AA}(p_T) \approx \int dx P(x)(1-x)^{n(p_T)-1} \tag{2}$$

where $P(x)$ is probability of losing the fractional energy of x and n is slowly varying function of p_T that can be determined experimentally. Equation (2) provides us with theoretical access to the R_{AA} observable and its calculation will form as the main focus of this project. Section 3 will discuss the modeling of the $P(x)$ distribution in eq. (2).

To get an intuitive feeling for eq. (2) we can check two extreme energy loss cases and see that we get the expected results. If we consider a particle that loses no energy, the R_{AA} should just be one. The $P(x)$ distribution associated to a particle that loses no energy would just be a delta centred at

$x = 0$, as the probability of losing a fraction of momentum x will have no support other than at zero. We see that if we let $P(x) = \delta(x)$ we get

$$R_{AA} = \int dx \delta(x)(1-x)^{n-1} = 1 \tag{3}$$

exactly as we would expect. The other extreme case would be a particle that loses all of its energy, the $P(x)$ distribution associated to this scenario would just be a delta centred at $x = 1$. Letting $P(x) = \delta(x-1)$ we get

$$R_{AA} = \int dx \delta(x-1)(1-x)^{n-1} = 0 \tag{4}$$

and a R_{AA} of 0 is exactly what we would expect if a particle were to lose all of its energy.

2.1 Geometry Average of the R_{AA}

The QGP that forms in a collision can take on a variety of geometrical structures, which, for instance are dependent on the centrality of the collision or the parent nuclei involved in the collision. The drop of QGP that forms in collisions also has a dynamic life of its own. The energy loss of the partons in the jets moving through the QGP will be dependent on the dynamics and the geometrical structure of the QGP.

Experimentally, we have access to the energy loss that occurs in the jets and not of the individual partons. Theoretically, QCD grants us access to the dynamics of the partonic structure. If our theoretical models have any chance of being comparable to data, must calculate the energy loss of the many partons that occur within a single jet. Which, as one can imagine, will become computationally very expensive as the partonic density increases within the jets.

In order to model the energy loss of the jets from the theoretically calculable partonic energy loss, we calculate the energy loss at the partonic scale for many different paths and then calculate an average R_{AA} for all the different paths, let us refer to this average R_{AA} for all the different paths as the *true average* and denote it as $\langle R_{AA} \rangle_t$. Each path is characterised by an entry point $(\mathbf{x})$ into the medium (we can think of this as the point where the parton begins its life) and direction ϕ in which the parton travels. The true average is calculated by assigning a weighting to the $R_{AA}(\mathbf{x}, \phi)$ of each particular partonic path; the weighted R_{AA} is then summed over to give the true average R_{AA}. The weighting we assign to each path is given by the number of binary collisions density n_{coll} (eq. (70)) and is only dependent on the entry point $\mathbf{x}$. The reason we weight by n_{coll} is because the number of hard scatters (which are the main contributors to the observed energy loss) scales like n_{coll} [25]. Formally, the true average is calculated as

$$\langle R_{AA} \rangle_t = \frac{\int d\phi d^2\mathbf{x} \quad R_{AA}(\mathbf{x}, \phi) n_{coll}(\mathbf{x})}{\int d\phi} \tag{5}$$

Of coarse, numerically we do not perform the integrals but rather we get an approximate form of

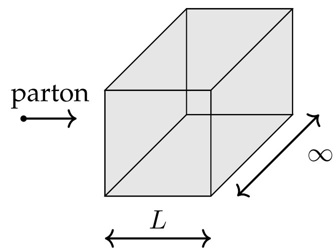

Figure 5: Depiction of the cube of quark gluon plasma used to calculate analytical expressions. In this depiction we imagine a parton that was created at the site of collision between two colliding nuclei; the parton has moved in direction transverse to the beam axis of the collision. Following the collision, the QGP forms after some finite time; the parton then enters the QGP and loses energy as it interacts with the medium.

eq. (5) by replacing the integrals with sums, *i.e.*

$$\langle R_{AA}\rangle_t \approx \frac{\sum_{\phi_i}\sum_{\mathbf{x}_j} \quad R_{AA}(\mathbf{x}_i,\phi_j)n_{coll}(\mathbf{x}_i)}{\sum_{\phi_i}} \tag{6}$$

2.2 Implementing the Geometry Average

Equation (6) was certainly easy to write down, but numerically this form of the geometric average is not tractable. Quite simply, this is because in order to perform the calculation prescribed in eq. (6) one would have to calculate the R_{AA} for every single path through the medium. Typically this would require ~ 20 angles and a grid of size $\sim 15 \times 15(\text{fm})^2$ with intervals of $\sim 0.05(\text{fm})$ to fully resolve the structure of the QGP formed in a single collision. If we would then like to average over many different collisions, which would we would need to in order to compare to experiment, we would have to calculate the R_{AA} another $\sim 10^3$ times. So a single R_{AA} data point would require $\sim 10^9$ R_{AA} calculations. On a standard laptop, calculating the R_{AA} for a single path takes about ~ 10 minutes of runtime, so to calculate the geometric average using eq. (6) would take ~ 50 years (again for just one data point). Numerically this task is quite simply impossible (even on a high performance computer).

In order to mitigate this computational expensiveness, we use an approximation and a clever trick. First we approximate the dynamics of the of QGP by assuming that it has no dynamics, *i.e.* it does not evolve with time. We then assume the QGP has a brick like structure (fig. 5) of length L with some temperature T (the specifics of how we assign these lengths and temperatures will be discussed in section 2.3). The clever trick is to then calculate the average of the R_{AA} by first finding a probability distribution (P_{LT}) for the different lengths and temperatures and then averaging over this distribution, we will term this method of calculating the average of the R_{AA} as the *geometric average* and denote it as $\langle R_{AA}\rangle_g$, quite simply this will take the form

$$\langle R_{AA}\rangle_g = \int dLdT \quad R_{AA}(L,T)P_{LT}(L,T) \tag{7}$$

In a rather satisfying fashion, the two methods I have described here are mathematically identical in the continuous limit (see appendix C.2)

The simplifications made to the structure of the QGP result in a minor speed up numerically and calculating the geometric average through P_{LT} has another important numerical speed up. The numerical speed up arises because the mapping which assigns the lengths and temperatures to the paths that the partons take through the medium is many to one. On-top of the many-to-one mapping, we can calculate different P_{LT} distributions for different collisions and then average over these different distributions instead of having to calculate the R_{AA} for each collision, this gives us another speed up of order $\sim 10^3$. This implies that we have to calculate significantly less R_{AA} as a function of L and T ($\sim 10^2$) than we would have to calculate for R_{AA} as a function of $\mathbf{x}$ and ϕ ($\sim 10^9$). Without the geometric averaging method, comparing our results to experiment is just not possible

2.3 Effective Lengths and Temperatures

In this section we will describe how the lengths and temperatures are assigned to the brick of QGP and how the probability distribution for the lengths and temperatures (P_{LT}) is calculated. This procedure of calculating the geometric average is common in the literature [26–29] and we shall refer to the procedure as the *effective length procedure* from here on. The individual lengths and temperatures we assign to the brick will be termed as *effective lengths* and *effective temperatures*.

As mentioned above, we shall simplify the structure of the QGP by assuming that the QGP has a brick-like form with some effective length and effective temperature. But we would like to closely approximate the actual dynamical and inherently complicated structure of the QGP with our brick model. We do this by assigning lengths and effective temperatures to the bricks that are larger for paths where more energy loss is expected to occur and smaller for paths where less energy loss is expected to occur. Partons that move through regions of the QGP that are dense will be likely to interact with the QGP medium more strongly and thus we should assign a larger length to the paths that go through more dense regions of the QGP. These considerations lead us to the following basic structure of an effective length [26, 29]:

$$L_{eff}(\mathbf{x}, \phi) = \frac{1}{N} \int_{\tau_0}^{\infty} d\tau \quad n(\mathbf{x} + \hat{\phi}\tau) \tag{8}$$

Where as before the parameter ϕ specifies the direction through which the parton travels and $\mathbf{x}$ specifies the starting point of the parton, n serves as a function which captures the density of the QGP, τ_0 is the formation time of the QGP, lastly N is a normalization constant. To be clear, eq. (8) is *general* structure for an effective length. In this project we varied how we normalize the lengths and also how we specified the density of the QGP[1].

We explored a variety of different effective length prescriptions, all of which are variants of eq. (8). The hopes were to find some uniformity in the predictions made by the different effective length prescriptions, and to find a variant which agreed well with experiment.

The density profiles of the QGP were modeled using either techniques from hydrodynmaics [31–

[1]The original form of eq. (8) used a Woods-Saxon nuclear density profile [30] to create participant transverse density $\rho_p(\mathbf{x})$. To match the notation of WHDG [29] with ours, we set $n = \rho_p$ and $N = \langle \rho_p \rangle$.

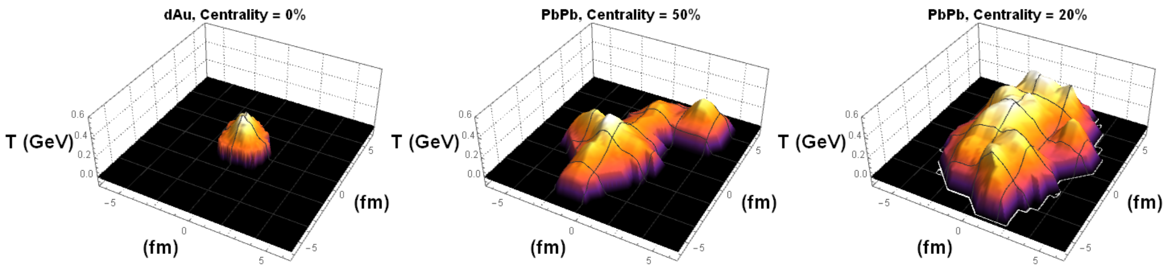

Figure 6: Hydrodynamical models for the temperature profile of QGP as a function of position from the collision site. From left to right the Profiles are for a dAu collisions at 0% centrality, and $PbPb$ collisions at 50% and 20% centrality respectively. More central collisions have temperature profiles that extend into larger regions of space, which corresponds to more QGP forming for these more central collisions.

38] or using the Glauber model [25]. Note that for the hydrodynamic models, we can immediately obtain an effective temperature from the normalization. When using the Glauber model for the effective length prescription, we use techniques from statistical mechanics to get an effective temperature (see appendix A.2). Below we present all six effective length prescriptions we explored.

Path Independent

$$L(\mathbf{x}, \phi, \tau_0) = \frac{1}{T^3_{eff}} \int_{\tau_0}^{\infty} dz T^3(\mathbf{x} + z\hat{\phi}, \tau_0) \tag{9}$$

$$T^3_{eff} = \left(\int d^2x T^6(\mathbf{x}, \tau_0) \right) \left(\int d^2x T^3(\mathbf{x}, \tau_0) \right)^{-1} \tag{10}$$

The *Path Independent* variant fixes the temperature distribution T at $t = \tau_0$ ($t = \tau_0$ is the formation time of the medium) and normalizes with T^3_{eff} by integrating over the entire static medium, *i.e.* the normalization is path independent.

Path Dependent

$$L(\mathbf{x}, \phi, \tau_0) = \frac{1}{T^3_{eff}(\mathbf{x})} \int_{\tau_0}^{\infty} dt T^3(\mathbf{x} + z\hat{\phi}, \tau_0) \tag{11}$$

$$T^3_{eff}(\mathbf{x}) = \left(\int_{\tau_0}^{\infty} dt T^6(\mathbf{x} + z\hat{\phi}, \tau_0) \right) \left(\int_{\tau_0}^{\infty} dt T^3(\mathbf{x} + z\hat{\phi}, \tau_0) \right)^{-1} \tag{12}$$

The *Path Dependent* variant again fixes the temperature distribution T at $t = \tau_0$ but now normalizes with T^3_{eff} by integrating through a particular path, *i.e.* the normalization is path dependent.

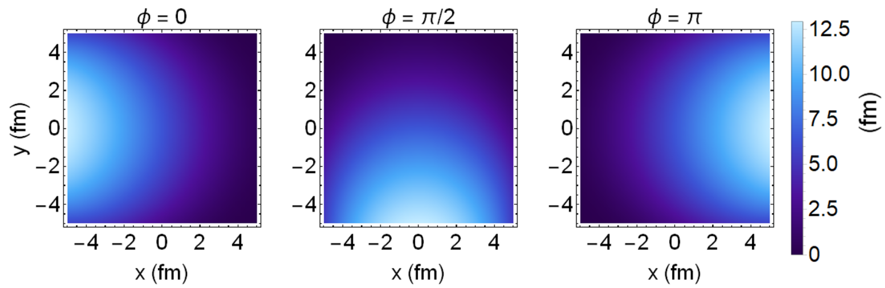

Figure 7: Effective lengths calculated in eq. (17) as a function of entry position $\mathbf{x}$ for a variety of different angles through the medium. The parton paths which enter through the most "dense" regions of the QGP correspond to larger effective lengths and thus will lose more energy. The color scale is determines the size of the length in *fm*.

Path Dependent - Bjorken

$$L(\mathbf{x},\phi,\tau_0) = \frac{1}{T^3_{eff}(\mathbf{x})}\int_{\tau_0}^{\infty} dt T^3(\mathbf{x}+z\hat{\phi},\tau_0)\frac{\tau_0}{t} \tag{13}$$

$$T^3_{eff}(\mathbf{x}) = \left(\int_{\tau_0}^{\infty} dt T^6(\mathbf{x}+z\hat{\phi},\tau_0)\left(\frac{\tau_0}{t}\right)^2\right)\left(\int_{\tau_0}^{\infty} dt T^3(\mathbf{x}+z\hat{\phi},\tau_0)\frac{\tau_0}{t}\right)^{-1} \tag{14}$$

This variant is similar to the *Path Dependent* prescription, except the temperature distribution now evolves with time through a Bjorken-like evolution ($\sim 1/t$)

Path Dependent - Pure Hydro

$$L(\mathbf{x},\phi,\tau_0) = \frac{1}{T^3_{eff}(\mathbf{x})}\int_{\tau_0}^{\infty} dt T^3(\mathbf{x}+z\hat{\phi},t) \tag{15}$$

$$T^3_{eff}(\mathbf{x}) = \left(\int_{\tau_0}^{\infty} dt T^6(\mathbf{x}+z\hat{\phi},t)\right)\left(\int_{\tau_0}^{\infty} dt T^3(\mathbf{x}+z\hat{\phi},t)\right)^{-1} \tag{16}$$

In the *Path Dependent - Pure Hydro* prescription, the time evolution of the medium is now governed by the full hydrodynamical simulation. This model of the effective length is the most sophisticated of the variants explored here.

The next two prescriptions for the effective length are similar to the path independent and path dependent prescriptions presented, the only difference is that the hydrodynimcal model for the temperature is switched out for the number of participants density (n_{part}) which can be defined by the Glauber Model and is discussed in appendix A.

Path Independent - Glauber Model

$$L(\mathbf{x}, \phi, \tau_0) = \frac{1}{\rho_{eff}} \int_{\tau_0}^{\infty} dz \quad n_{part}(\mathbf{x} + z\hat{\phi}, \tau_0) \tag{17}$$

$$\rho_{eff} = \left(\int d^2x \quad (n_{part})^2(\mathbf{x}, \tau_0) \right) \left(\int d^2x \quad n_{part}(\mathbf{x}, \tau_0) \right)^{-1} \tag{18}$$

Path Dependent - Glauber Model

$$L(\mathbf{x}, \phi, \tau_0) = \frac{1}{\rho_{eff}(\mathbf{x})} \int_{\tau_0}^{\infty} dt \quad n_{part}(\mathbf{x} + z\hat{\phi}, \tau_0) \frac{\tau_0}{t} \tag{19}$$

$$\rho_{eff}(\mathbf{x}) = \left(\int_{\tau_0}^{\infty} dt \quad \left(n_{part}(\mathbf{x} + z\hat{\phi}, \tau_0) \frac{\tau_0}{t} \right)^2 \right) \left(\int_{\tau_0}^{\infty} dt \quad n_{part}(\mathbf{x} + z\hat{\phi}, \tau_0) \frac{\tau_0}{t} \right)^{-1} \tag{20}$$

2.4 Probability Distributions for the Effective Lengths and Temperatures

For each effective length and temperature, a probability is assigned to the likelihood of the effective length and effective temperature occurring. This is the P_{LT} distribution mentioned in section 2.2. The prescription we use for assigning these probabilities is outlined as follows:

1. We evaluate the effective length and temperature (using one of the six models mentioned above) at some coordinate $\mathbf{x}$ (which represents the entry point of the parton into the medium) and in some direction ϕ (which specifies the direction of travel through the QGP).

2. For each direction ϕ and position $\mathbf{x}$, we weight the effective length and temperature by the number of collisions density to obtain a spread of data of the form $n_{coll}(\mathbf{x})$ vs ($L_{eff}(\mathbf{x})$,$T_{eff}(\mathbf{x})$)

3. From here, we then bin the $n_{coll}(\mathbf{x})$ vs ($L_{eff}(\mathbf{x})$,$T_{eff}(\mathbf{x})$) data and normalize it to obtain a probability distribution for our effective lengths and temperatures.

Formally, the prescription for P_{LT} can be summarized in the following expression:

$$P_{LT}(L_{eff}, T_{eff}) = \frac{\sum_{\phi_i} \sum_{\mathbf{x}_i : L_{eff}(\mathbf{x}_i, \phi_i) = L_{eff}} \sum_{\mathbf{x}_i : T_{eff}(\mathbf{x}_i, \phi_i) = T_{eff}} n_{coll}(\mathbf{x}_i)}{\sum_{\phi_i}} \tag{21}$$

The condition $\mathbf{x}_i : L_{eff}(\mathbf{x}_i, \phi_i) = L_{eff}$ in the summation should be read as a trigger that only activates when the path through the medium results in a length of L_{eff} and similarly for the condition in the T_{eff} summation.

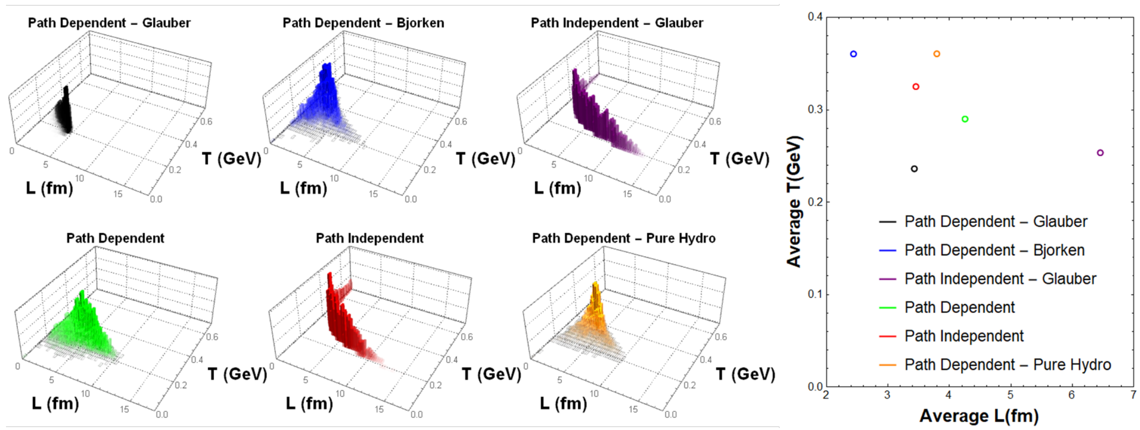

Figure 8: (Left) Probability distributions of effective lengths and temperatures for different effective lengths models. Note the strong correlation between temperature and length in the probability distributions for the Glauber model and the Path Independent model. In the Glauber model case, the strong correlation comes from eq. (83) which defines the temperature in terms of the lengths. Similarly, for the Path Independent model, there is a direct relation between lengths and temperatures which comes from eq. (10). The other models do not have one-to-one mappings and thus their lengths are not strongly correlated to their temperatures. (Right) Two-dimensional average of each of the probability distributions. Notice the disparate averages for each of the probability distributions.

3

Energy Loss Model

In this section we will discuss how the incoming patrons lose their energy and how we calculate this energy loss. As the partons move through the QGP, they lose energy by interacting with the medium. The energy loss can occur via two mechanisms. One of these energy loss mechanisms is radiative; the radiation is a result of the partons moving through the plasma and emitting energy (*bremsstrahlung*) as they decelerate. The energy that is emitted, is transferred in the form of gluons (the mediators of the strong force). The second energy loss mechanism is an elastic energy loss. The elastic energy loss occurs as the incoming patrons collide with other particles in the medium and as a result transfer some their energy. The total energy loss would then be the sum of the two energy loss mechanisms.

All analytical expressions are derived under the assumption that the QGP that forms after a collision is in the shape of a brick. This brick of QGP is infinite in the direction transverse to the direction of the incoming parton and finite in the direction longitudinal to the incoming parton (see fig. 5). This simplified shape of the QGP allows the energy loss expressions obtained to be tractable.

3.1 Radiative Energy Loss of a Single Gluon Emission

The initial wavefunction of the colliding nuclei in AA collisions are of exceedingly complicated forms and thus any calculations in pQCD or lattice QCD are intractable. The resolution to this complexity, is to introduce an effective theory in which one can calculate the dynamics of the partons as they move through the QGP. These effective theories endeavour to calculate the probability distribution of fractional energy loss due to a single gluon emission occurring; the probability distributions are known as single gluon emission kernels. Once the single gluon emission kernel is obtained, one can then assume that the number of emissions are independent from each other; this allows the introduction of a Poisson distribution to include the effects of multiple gluons being emitted [39].

There are many different radiative energy loss formalisms that are applicable under different physical assumptions, such as Baier-Dokshitzer-Mueller-PeigneSchiff-Zakharov (BDMPS-Z), Arnold-Moore-Yaffe (AMY), higher twist (HT), and developments in ADS-CFT correspondence have been utilized in describing the energy loss. Reviews on these methods can be found in [2, 40–42]. We shall work under the formalism developed by Djordjevic-Gyulassy-Levai-Vitev (DGLV) [3] which is an extension of the formalism devolved in the work done by GLV [43].

It should be noted that we are working under the assumptions that the Eikonal approximation and the soft gluon approximation hold true. The Eikonal approximation assumes that the energy of the incoming parton sets the largest scale of the energy loss in the set up, while the soft gluon approximation makes the assumption that the fraction of momentum of the incoming parton that is carried away by the radiated gluon (x) is small.

3.1.1 Expansion in Opacity

The opacity of a medium is defined as L/λ where L is the length of the medium and λ is the mean free path of a particle traveling through the medium. The opacity gives one a measure of how many interactions will occur between a particle and the medium through which it travels. The energy loss expressions in the DGLV formalism of the parton moving through the QGP will be derived from an expansion in the opacity of the QGP. Derivations of the energy loss can be found in [44]; the derivations are performed under the assumption that the scattering with the medium is in the limit of a single hard and co-linear scatter and we are make use of a large formation time approximation, which allows one to work up to first order in the opacity expansion.

3.1.2 Notation and Set Up

Let us define the notation we will be using in this project, we will keep the same conventions as those found in [27]. $C_A = 3$ and $C_R = 4/3$ are the Casimir in the gluon representation [45] and the Casimir in a representation related to the leading parton respectively while α_s is the strong coupling constant. The two momenta $\mathbf{k}$ and $\mathbf{q}$ are the transverse momentum of the radiated gluon and the transverse momentum exchanged between the radiated gluon and the medium respectively. We also have that M is the mass of the incident parton, L is the length of the brick of QGP, μ is the Debye mass and $m_g = \mu/\sqrt{2}$ is the mass of the gluon which is obtained by taking into the QCD analogue of the Ter-Mikayelian plasmon effect [46](see appendix B.1.2). The quatity described by $\tilde{\rho}(\Delta z)$ is the density of scattering sites in the medium. The scattering centre density can be thought of as the density of the medium through which the parent parton is moving, each scattering centre can be seen as a static parton which the parent parton could potentially interact with. The scattering centre is assumed to be described by a Gyulassy-Wang Debye screened potential [47]. Lastly, ϵ is the polarization of a massless boson[2]. We will make use of the following short-hand to simplify our expressions

$$
\begin{aligned}
\omega &= xE \\
\omega_0 &= \mathbf{k}^2/2\omega \\
\omega_1 &= (\mathbf{k}-\mathbf{q})^2/2\omega \\
\tilde{\omega} &= (m_g^2 + M^2x^2)/2\omega
\end{aligned}
$$

[2]One should note that $\epsilon^\mu = (0, \epsilon)$ and $\epsilon_\mu \epsilon_\nu = -g_{\mu\nu}$, where $g_{\mu\nu}$ is the Minkowski metric. This implies that terms like $(\epsilon \cdot \mathbf{k})(\epsilon \cdot \mathbf{q})$ evaluate to $\mathbf{k} \cdot \mathbf{q}$.

With these conventions in place, the radiative energy loss of a single gluon emission takes the form

$$\begin{aligned}\frac{dE_{rad}}{dx} = \frac{C_R \alpha_s L E}{\pi} \int \frac{d^2\mathbf{q}}{\pi} \frac{\mu^2}{\lambda\left(\mu^2+\mathbf{q}^2\right)^2} \int \frac{d^2\mathbf{k}}{\pi} \int d\Delta z \tilde{\rho}(\Delta z) \\ \times \left[-\frac{2\left(1-\cos\left\{\left(\omega_1+\tilde{\omega}_m\right)\Delta z\right\}\right)}{\left(\mathbf{k}-\mathbf{q}\right)^2+m_g^2+x^2M^2} \left(\frac{(\mathbf{k}-\mathbf{q})\cdot\mathbf{k}}{\mathbf{k}^2+m_g^2+x^2M^2} - \frac{\left(\mathbf{k}-\mathbf{q}\right)^2}{\left(\mathbf{k}-\mathbf{q}\right)^2+m_g^2+x^2M^2} \right) \right. \\ + \frac{1}{2} e^{-\mu_1 \Delta z} \left\{ \left(\frac{\mathbf{k}}{\mathbf{k}^2+m_g^2+x^2M^2} \right)^2 \left(1-\frac{2C_R}{C_A}\right) \left(1-\cos\left\{\left(\omega_0+\tilde{\omega}_m\right)\Delta z\right\}\right) \right. \\ \left. \left. + \frac{\mathbf{k}\cdot(\mathbf{k}-\mathbf{q})\left(\cos\left\{\left(\omega_0+\tilde{\omega}_m\right)\Delta z\right\}-\cos\left\{\left(\omega_0-\omega_1\right)\Delta z\right\}\right)}{\left(\mathbf{k}^2+m_g^2+x^2M^2\right)\left(\left(\mathbf{k}-\mathbf{q}\right)^2+m_g^2+x^2M^2\right)} \right\} \right].\end{aligned} \tag{22}$$

The second line along with the prefactor in the first line in eq. (22) is the radiative energy loss derived by DGLV [3] and we shall refer to its contribution as *DGLV* contribution. The third and fourth lines, again along with the prefactor, is the short path length correction to the energy loss derived by Kolbe and Horowitz [27] and we shall refer to its contribution as the *SPLC* contribution. To be explicit, we separate the two contributions as

$$\frac{dE_{rad}}{dx} = \frac{dE_{DGLV}}{dx} + \frac{dE_{SPLC}}{dx} \tag{23}$$

3.1.3 Total Energy Loss and the Single Gluon Emission Kernel

We can find the total radiative energy loss by integrating out x

$$\Delta E = \int_0^1 dx \frac{dE_{rad}}{dx} = \Delta E_{DGLV} + \Delta E_{SPLC} \tag{24}$$

Note that the bounds of the integrals run from 0 to 1 as x is the fraction of momentum loss due to radiation and as such cannot extend negatively beyond zero.

To derive an expression for the single gluon emission kernel we note that the total energy lost during radiation is equal to the the number of radiated gluons (N^g) multiplied by the fractional energy carried away (x) by each radiated gluon.

$$dE_{rad} = xE dN^g \tag{25}$$

$$\implies \frac{dN^g}{dx} = \frac{1}{xE}\frac{dE_{rad}}{dx} \tag{26}$$

We can then find the number of radiated gluons by integrating out the x dependency, we will interpret this as the *average* number of gluon emissions.

$$\begin{aligned} N^g &= \int_0^1 \frac{dN^g}{dx} \\ &= \int_0^1 \frac{1}{xE}\frac{dE_{rad}}{dx} \end{aligned} \tag{27}$$

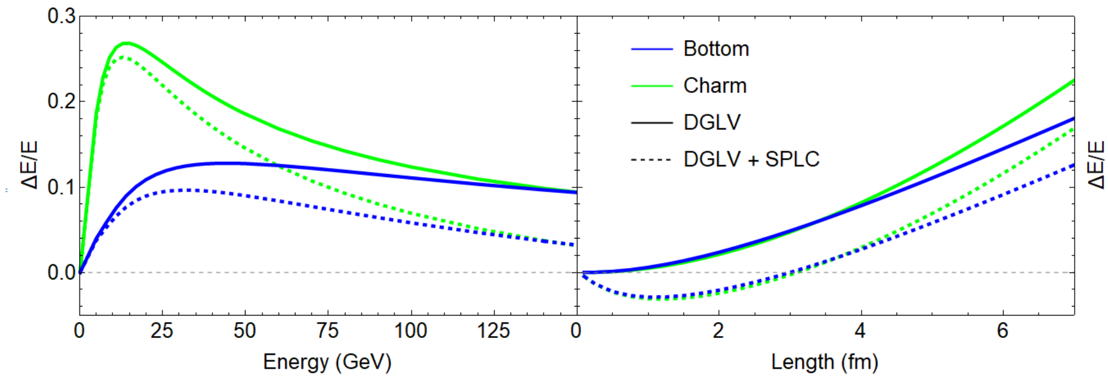

Figure 9: A comparison between the predictions made by the DGLV and DGLV + SPLC models for the fractional energy loss (eq. (24)) for charm (mass = 1.2GeV) and bottom (mass = 4.75GeV) quarks. The left panel shows the fractional energy loss as a function of the incident energy of the incoming quark. The right hand panel shows the fractional energy loss as a function of the path length of the incident quark moving through the QGP medium. The differences between the corrected and uncorrected terms become more important at higher energies. The curves are calculated with the parameters $T = 0.25$ GeV, $L = 5$ fm (for the left panel) and $E = 100$ GeV (for the right panel) while the μ and λ parameters can be found from eq. (84) and eq. (87) respectively. Notice the negative energy loss for $L < 3$ fm, this suggests that the energy loss in the medium is less than energy loss that would have occurred in the vacuum as all calculations are done relative to the vacuum.

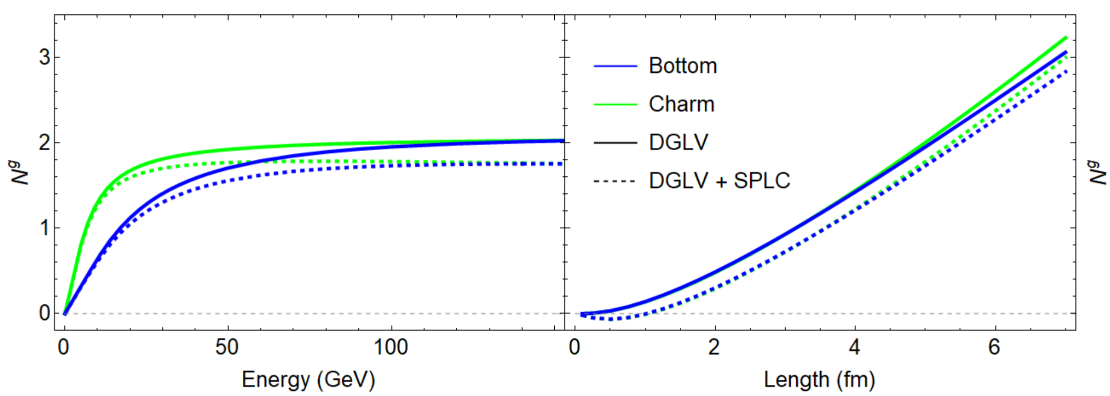

Figure 10: The right hand panel shows the result of eq. (27) for $E = 100$ GeV for bottom and charm quarks while the left hand panel displays the average number of gluons emitted as a function of length with $L = 5$ fm. Both figures were calculated with $T = 0.25$ GeV. Notice the negative number of gluon emissions for $L < 1$ fm, this suggests that the number of gluons being emitted in the medium is less than the number of emissions that would have occurred in the vacuum since all calculations are done relative to the vacuum.

3.2 Elastic Energy Loss of a Single Collision

The original developments made by WHDG calculated elastic energy loss using the Braaten and Thoma (BT) approach [48]. Briefly, this approach makes use of two asymptotic energy regimes to find expressions for the form of the elastic energy loss; $E \ll M^2/T$ and $E \gg M^2/T$ where M is the mass of the incident parton and T is the temperature of the medium. The two results for the different asymptotic regions are then stitched together using a matching function which is a smooth function satisfying the constraints of BT.

More recent developments by [26, 49] perform the elastic energy loss calculations using an effective theory called Hard Thermal Loops (HTL). In short HTL takes into account screening affects by giving the gluon a mass, resulting in effective gluon propagators which are infrared shielded. Here, we will just quote some the key results needed to compute the elastic energy loss.

The interaction rate dN^c/dz, where N^c is the number of elastic scatters and z is the distance that the parton has traveled through the medium can be written as

$$\begin{aligned}\frac{dN^c}{dz} =& \frac{4C_R\alpha_s^2}{\pi}\int\frac{d^3Qd\omega}{2\pi}\frac{E}{E'}\delta\left(\omega+E-E'\right)\frac{n_B(\omega)}{Q}\left(1-\frac{\omega^2}{Q^2}\right)^2 \\ &\times\left\{\sum_m\left[C^m_{LL}\left|\Delta_L\right|^2+2C^m_{LT}\,\mathrm{Re}\left(\Delta_L\Delta_T\right)+C^m_{TT}\left|\Delta_T\right|^2\right]\right\}\end{aligned} \tag{28}$$

here Δ_L and Δ_T are the longitudinal and transverse propagators, while $n_B(\omega)$ is the Bose distribution and $\omega = xE$ and $Q = \omega/x$ with x the fractional energy loss and E the energy of the incoming parton.The C^M_{IJ} coefficients are defined as

$$C^m_{IJ} = \int_{\frac{1}{2}(\omega+Q)}^{\infty} k^0kdk\left(n_m\left(k^0-\omega\right)-n_m\left(k^0\right)\right)c'_{IJ} \tag{29}$$

here the c'_{IJ} coefficients are defined as

$$c'_{LL} \equiv \left(\left(1+\frac{\omega}{2E}\right)^2-\frac{Q^2}{4E^2}\right)\left(\left(1-\frac{\omega}{2k^0}\right)^2-\frac{Q^2}{4\left(k^0\right)^2}\right) \tag{30}$$

$$c'_{LT} \equiv 0 \tag{31}$$

$$c'_{TT} \equiv \frac{1}{2}\left(\left(1+\frac{\omega}{2E}\right)^2+\frac{Q^2}{4E^2}-\frac{1-v^2}{1-\frac{\omega^2}{Q^2}}\right)\left(\left(1+\frac{\omega}{2k^0}\right)^2+\frac{Q^2}{4\left(k^0\right)^2}-\frac{1-v_k^2}{1-\frac{\omega^2}{Q^2}}\right) \tag{32}$$

where $v_k(v)$ is the velocity of the incoming parton. The C^M_{IJ} coefficients can be calculated analytically using the following thermal integrals

$$I^m_n \equiv \int_{\frac{1}{2}(\omega+Q)}^{\infty} dk\left(n_m(k-\omega)-n_m(k)\right)k^n \tag{33}$$

For bosons $(+)$ and fermions $(-)$ respectively, these evaluate to

$$\begin{aligned}I^{\pm}_0 &= \pm T\log\left(\frac{1\mp e^{-\kappa_+}}{1\mp e^{-\kappa_-}}\right) \\ I^{\pm}_1 &= \pm T^2\left[\mathrm{Li}_2\left(\pm e^{-\kappa_-}\right)-\mathrm{Li}_2\left(\pm e^{-\kappa_+}\right)\right]+\kappa_+TI^{\pm}_0 \\ I^{\pm}_2 &= \pm 2T^3\left[\mathrm{Li}_3\left(\pm e^{-\kappa_-}\right)-\mathrm{Li}_3\left(\pm e^{-\kappa_+}\right)\right] \\ &\quad + 2\kappa_+TI^{\pm}_1-\kappa_+^2T^2I^{\pm}_0\end{aligned} \tag{34}$$

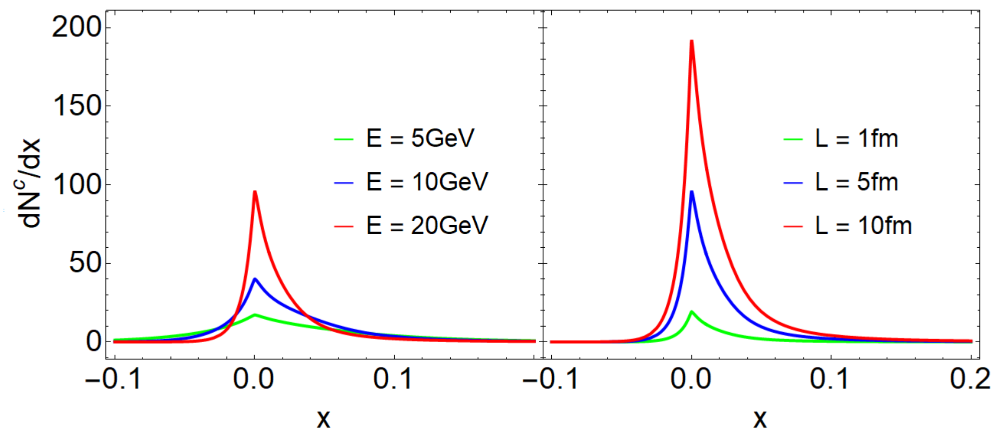

Figure 11: (Left) Equation (35) for bottom quarks with a constant temperature of 0.25 GeV and a fixed length of 5 fm. (Right) Equation (35) for bottom quarks with a constant temperature of 0.25 GeV and a fixed energy of 20 GeV. All the z dependence in eq. (35) comes from the temperature distribution, which in this case is constant, thus eq. (35) becomes eq. (36)

where Li_n is the polylogarithm function and we have defined $k_\pm = (\omega \pm Q)/2T$ with T the temperature of the medium. Lastly we perform a change of variables from ω to x with to convert the scattering rate in eq. (28) to a single elastic scattering kernel.

$$\begin{aligned} \frac{dN^c}{dx} &= \frac{d\omega}{dx}\frac{d}{d\omega}\int dz \frac{dN^c}{dz} \\ &= E\frac{d}{d\omega}\int dz \frac{dN^c}{dz} \end{aligned} \tag{35}$$

Previous applications in [26, 49] assumed that the scattering rate was independent of z allowing them to write elastic scattering kernel as

$$\frac{dN^c}{dx} \simeq LE\frac{dN^c}{dzd\omega} \tag{36}$$

which would be true for the case of a static brick. We will explore some of the effects of dropping this static brick assumption in both the elastic and radiative energy loss kernels in section 4. Similarly to the radiative energy loss, we can define the define elastic energy loss through the number of scatters *viz.*

$$\Delta E^c = \int_{-\infty}^{1} \frac{dE^c}{dx} \tag{37}$$

with the following expression for dE^c/dx

$$\frac{dE^c}{dx} = xE\frac{dN^c}{dx} \tag{38}$$

The only key difference between eq. (24) and eq. (37) is that the integral bounds run from 0 to 1 in the radiative case, as it would be un-physical for a gluon to radiate negative energy, but there is no physical constraint which prevents a parton from gaining energy in a collision and hence losing a *negative* amount of energy.

3.3 Multiple Emissions and Multiple Collisions

Insection 3.1 and section 3.2 we wrote down the single gluon emission (dN^g/dx) and single collision kernels (dN^c/dx) respectively; the two kernels can be thought of as probability distributions (once we normalize them) for the amount of fractional energy loss (x) occurring in the case of a single gluon emission and a single collision respectively. However, we are interested in finding the gluon emission (collision) kernels for any number of emissions (collisions). This can be done by making two further assumptions. The first is that the number of emissions (collisions) are independent from one another; that is to say that in the event of n emissions (collisions) occurring for a parton, then the probability of n' emissions (collisions) occurring for another parton is unchanged. The second assumption, perhaps more dubious than the first, lies in an analogy between QED and QCD. Namely, in QED photon radiation exactly follows a Poisson distribution in the case that the radiated energy of the electron is much less than its incoming energy [50]. The Poisson distribution is a probability distribution of the form

$$P(n) = \frac{\lambda^n e^{-\lambda}}{n!} \tag{39}$$

and the distribution gives one probability that n events will occur given that the average number of events occurring is λ. We assume, as done in [39], that the number of gluons emitted also follows a Poisson distribution and we do the same for the number of collisions.

We write the (normalized) probability distributions for the fractional momentum loss a single emission and single collision as

$$p_1^{rad}(x) := \frac{1}{N^g}\frac{dN^g}{dx} \tag{40}$$

$$p_1^{el}(x) := \frac{1}{N^c}\frac{dN^c}{dx} \tag{41}$$

respectively. After successive convolutions and after accounting for the probability leakage that comes from restricting our integral domains to cut-off at $x = 1$, we get the following expressions for the probability distributions for the fractional momentum loss of multiple emissions and multiple collisions

$$\tilde{P}_{rad}(x) = \sum_{n=0}^{\infty} \frac{(N^g)^n}{n!} e^{-N^g} p_n^{rad}(x) + W_{rad}\delta(x-1) \tag{42}$$

$$\tilde{P}_{el}(x) = \sum_{n=0}^{\infty} \frac{(N^c)^n}{n!} e^{-N^c} p_n^{el}(x) + W_{el}\delta(x-1) \tag{43}$$

here p_n^{rad} is the probability that n gluons will be emitted while $p_n^{el}(x)$ is the probability that n collisions will occur. The details of the derivations of eq. (42) and eq. (43) can be found in appendix B.2. Armed with eq. (42) and eq. (43) one can obtain the probability distribution for the total energy loss by convolving $\tilde{P}_{rad}$ with $\tilde{P}_{el}(x)$, we state it here for completeness.

$$P_{tot}(x) = \int dy \quad \tilde{P}_{el}(y)\tilde{P}_{rad}(x-y) \tag{44}$$

P_{tot} is the probability distribution we will use in eq. (2) to calculate the R_{AA}.

3.4 Results and Discussion

The effective length and temperature procedure for calculating an geometrically averaged R_{AA} that is common practice in the literature [3, 26, 27, 29, 43, 44, 51] has been described in this chapter. As a development to what has already been done in the field, we presented a variety of different ways of calculating the effective lengths and temperatures in section 2.3; each method differed from another by varying either the path dependency or the normalization. It is important to note that the different effective length and temperature models were all motivated in the ultimate goal to speed up the numerical challenges encountered in calculating an R_{AA}. The models are not directly related to any physical theory, but rather they form as an extension to the physical model that are required to get numerical results. As such, for these different models to be introduced into our R_{AA} calculations with any form of confidence, we require that the effects that the models have in differing from the *true prediction* made would be marginal, here the true prediction would be result of the *true average* described in section 2.1. As mentioned there, the true average is numerically expensive and this motivated the introduction of the geometric average. Only if the deviations from the true predication made were small, could we regard our modeling procedure as a success, and only then could we actually begin to trust the results of the effective length and temperature procedure.

The results of the effective length and temperature procedure however, do not meet these minimal requirements for a successful model. The first sign of the effective length and temperature procedure breaking down arises in the probability distributions we obtain for the effective length and temperatures fig. 8. The distributions we obtain differed from each other significantly, not only in their global shape, but (more detrimental to the success of the effective length and temperature procedure) also in their first moments for the temperatures and lengths.

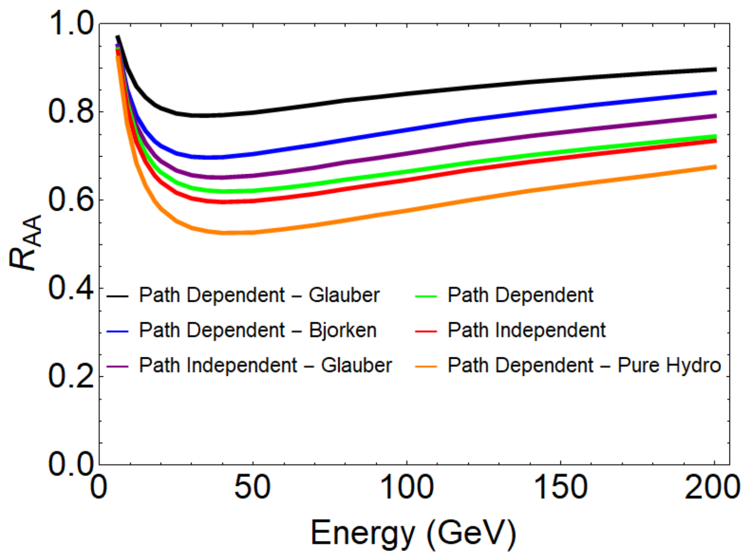

Figure 12: Geometric averaged R_{AA} as a function of the energy of the incoming parton for each of the different effective length and temperature models described in section 2.3. The striking feature of this result is the large range of results spanned by the different models.

The final results we get for the geometrically averaged R_{AA} will be highly dependent on the probability distribution (which encodes the geometry of the QGP) that is being averaged over. The different effective length and temperature models all give vastly different probability distributions, and thus the R_{AA} prediction that they make are also highly disparate as evident in fig. 12. This clearly highlights the lack of robustness in the effective length procedure as there is no uniform convergence in the predictions made by the different models.

4

Modifications to the Energy Loss Model

In the previous chapter the R_{AA} was calculated under the assumption that the QGP forms as a simplified brick-like structure. This simplification was introduced purely on the grounds that it provided a numerical advantage in the R_{AA} calculation. This simplification is common practice in the literature [3, 26, 27, 29, 43, 44, 51]. In the process of simplifying the geometry of the QGP, an effective length and temperature were introduced into the calculation. We showed that varying the manor in which the effective lengths and temperatures are assigned to the brick of QGP resulted in a wide range of R_{AA} predictions (see fig. 12). As a result, we can conclude that the procedure of assigning an effective length and temperature to the brick of QGP is not as robust as one would need to have faith in the predictions made by the model.

In this chapter we shall explore a modification made to the DGLV energy loss model. In summary, the modification will no longer use the brick simplification but instead, the structure of the QGP will be modeled using hydrodynamics and thus the geometry of the QGP will now have a dynamic and more physical form. The hydrodynamic form of the QGP (which we shall refer to as the *true geometry* of the QGP) will then be fitted with a two parameter power-law function, we will refer to this as the *fitted geometry*. The R_{AA} will then be calculated as a function of these two parameters and then, similarly to the geometric averaging in section 2.1, the R_{AA} will be averaged over the two parameters, we shall refer to this procedure of calculating the geometric average of the R_{AA} as the *fitted parameters procedure* to distinguish it from the *effective length and temperature* procedure discussed in the previous sections.

4.1 Modeling the Geometry of the QGP

Previous work [3, 26, 27, 29, 43, 44, 51] in the field had modeled $\bar{\rho}$ (which forms as a probability distribution for the number of scattering cites) in eq. (22) as a brick-like structure taking the form of an exponential decay

$$\bar{\rho}(\Delta z) = \frac{L}{2} \exp\left(\frac{-\Delta z}{(L/2)}\right) \tag{45}$$

or a step function

$$\bar{\rho}(\Delta z) = \frac{1}{L}\theta(z - L) \tag{46}$$

other similar variants have been explored. We now move away from this simplifying assumption by including the true geometry of the QGP into our calculations. Following the work of Kolbe [44], we can write the scattering centre probability distribution ($\bar{\rho}$) in terms of a density (ρ), for the number of

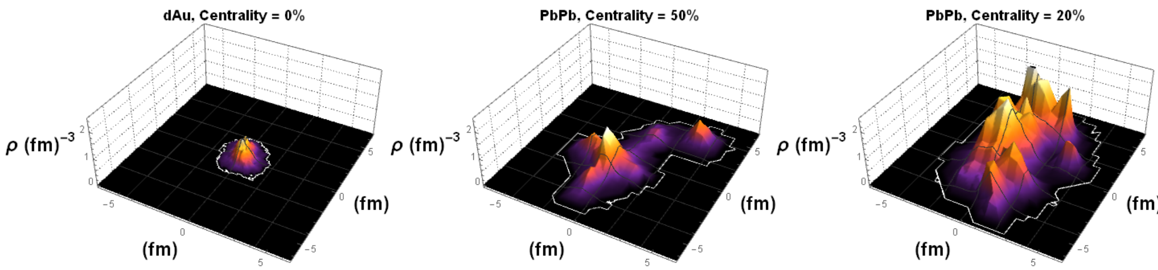

Figure 13: From left to right the density profiles of eq. (48) are for a dAu collision at 0% centrality, and $PbPb$ collision at 50% and 20% centrality respectively. More central collisions have density profiles that extend into larger regions of space, which corresponds to more QGP forming for these more central collisions.

scattering centres through the following relation

$$\rho = \frac{\mu^2 L}{(9/2)\pi\alpha_s^2\lambda}\bar{\rho} \tag{47}$$

Following the work of [24], we can write down an expression for the scattering center (ρ) in terms of a hydrodynamical temperature distribution as

$$\rho(t, \mathbf{x}) = \frac{4\zeta(3)(4 + n_f)}{\pi^2} T^3(t, \mathbf{x}) \tag{48}$$

Here, n_f is the number of the number of active quark flavours, which is taken to be 2 throughout this manuscript as only the charm and bottom quark contribute to the observed spectra at the energy scales at which we are concerned; $\zeta(3) \approx 1.202$ where ζ is the Riemann zeta function. Equation (48) allows us to model the true geometry of the QGP, the geometry now evolves with time and has a rich structure (see fig. 13). We provide a derivation of eq. (48) in appendix A.2.

The dynamics of ρ are encoded in the dynamics that arise from the hydrodynamical model of the temperature distribution T. A few examples of the hydrodynamic temperature distributions are shown in fig. 6.

Note that in what follows, we shall write $T(z)$ for the hydrodynamic temperature distribution, this is a shorthand and it refers to a specific path through the hydrodynamic temperature distribution which is a function of the coordinate $\mathbf{x}$ and the time t after formation, *i.e.* $T = T(t, \mathbf{x})$. So one should read $T(z)$ as $T(z) = T(z, z\cos(\phi) + x_0, z\sin(\phi) + y_0)$ where ϕ specifies the angle through the medium which the particular path is following and $\mathbf{x}_0 = (x_0, y_0)$ is the entry point into the medium.

4.1.1 Fitting the Hydrodynamics

Now, to each path through the medium we have a scattering centre ρ from eq. (48). So for each path through the medium we can calculate the energy loss using a similar formalism to that of section 3 (with some modifications to be discussed in section 4.2.1). Of coarse, as discussed in section 2.2 this will be numerically very challenging, even more so as the geometry of the QGP is no longer in its simplified brick form. To circumvent these numerical challenges, we introduce the fitting parameters

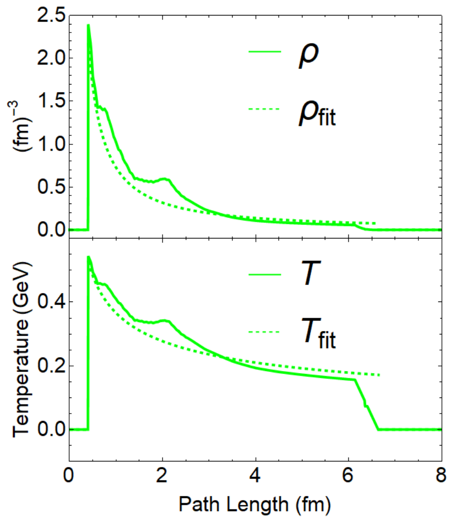

Figure 14: (Left) Comparison of hydrodynamic temperature distribution and the *fitted* temperature distribution from eq. (51). (Right) Comparison of hydrodynamic scattering centre eq. (48) and the *fitted* scattering centre from eq. (49). Here the hydrodynamic temperature distribution is generated from a *PbPb* collision at 20% centrality. The α parameter is fixed at 1.2 and for this particular path, ρ_0 was found to be 0.727 $(\text{fm})^{-1.8}$ while z_c was found to be 6.64 fm.

ρ_0 and z_c and fit eq. (48) for each path through the medium via the following power-law

$$\rho_{fit}(z, \rho_0, z_c) = \frac{\rho_0}{z^\alpha}\theta(z_c - z)\theta(\tau_0 - z) \tag{49}$$

Similarly to the effective length and effective temperature procedure, we will find that the map from the paths to the fitted parameters is many to one. This will mean that (as was the case for the effective length and effective temperature procedure) we will need to calculate the energy loss significantly less to get an average R_{AA} that is comparable to data. In eq. (49), θ is the Heaviside function and τ_0 is the formation time of the medium which we took to be $\tau_0 = 0.4fm$ for all calculations. The α parameter gave the best results in this model when $\alpha = 1.2$ and is from here on fixed. The ρ_0 and z_c parameters are free. Each hydrodynamical path has critical temperature, below which the temperature is taken to be zero. This critical temperature serves as the motivation for the z_c parameter. Specifically z_c is the distance traveled along the particular path at which the thermalization occurs. In order to fix the ρ_0 parameter we ensure that the following condition is satisfied

$$\int_{\tau_0}^{\infty} dz T(z) \stackrel{!}{=} \int_{\tau_0}^{\infty} dz T_{fit}(z) \tag{50}$$

where T_{fit} is defined as

$$T_{fit}(z, \rho_0, z_c) = \left(\frac{\pi^2}{4\zeta(3)(4 + n_f)} \rho_{fit}(z, \rho_0, z_c) \right)^{1/3} \tag{51}$$

4.2 Energy Loss

Here we will discuss some of the key differences between energy loss calculations for the effective length and temperature procedure and the energy loss calculations for the fitted parameter procedure.

4.2.1 Radiative Energy Loss

Writing eq. (22) in terms of eq. (47), the energy loss formalism becomes independent of the effective length, L. We consider the DGLV energy loss term and the short path length correction term separately; the DGLV term takes the following form

$$\begin{aligned}\frac{dE_{DGLV}}{dx} &= \frac{9C_R\alpha_s^3 E}{2}\int d\Delta z\rho(\Delta z)\int\frac{d^2\mathbf{q}}{\pi}\frac{1}{(\mathbf{q}^2+\mu^2)^2}\int\frac{d^2\mathbf{k}}{\pi}\\ &\times\frac{-2(\epsilon\cdot(\mathbf{k}-\mathbf{q}))}{(\mathbf{k}-\mathbf{q})^2+m_g^2+M^2x^2}\left[1-\cos\left\{(\omega_1+\tilde{\omega}_m)\,\Delta z\right\}\right]\\ &\times\left[\frac{\epsilon\cdot\mathbf{k}}{\mathbf{k}^2+m_g^2+M^2x^2}-\frac{\epsilon\cdot(\mathbf{k}-\mathbf{q})}{(\mathbf{k}-\mathbf{q})^2+m_g^2+M^2x^2}\right]\end{aligned} \tag{52}$$

While, the correction term can now be written as

$$\begin{aligned}\frac{dE_{SPLC}}{dx} &= \frac{9C_R\alpha_s^3 E}{2}\int d\Delta z\rho(\Delta z)\int\frac{d^2\mathbf{q}}{\pi}\frac{1}{(\mu^2+q^2)^2}\int\frac{d^2\mathbf{k}}{\pi}\frac{e^{-\sqrt{\mu^2+q^2}\Delta z}}{2}\\ &\times\left\{\frac{\mathbf{k}^2}{(\mathbf{k}^2+m_g^2+M^2x^2)^2}\left(1-\frac{2C_R}{C_A}\right)(1-\cos\left\{(\omega_0+\tilde{\omega}_m)\,\Delta z\right\})\right.\\ &+\left.\frac{\mathbf{k}\cdot(\mathbf{k}-\mathbf{q})\left[\cos\left\{(\omega_0+\tilde{\omega}_m)\,\Delta z\right\}-\cos\left\{(\omega_0+\tilde{\omega}_1)\,\Delta z\right\}\right]}{(\mathbf{k}^2+m_g^2+M^2x^2)((\mathbf{k}-\mathbf{q})^2+m_g^2+M^2x^2)}\right\}\end{aligned} \tag{53}$$

Note that as additional extension to the DGLV model we have included a temperature dependence into the Debye mass (μ), and the mass of the gluons (m_g), the exact relations for the explicit temperature dependence can be found in appendix A.2.

4.2.2 Elastic Energy Loss

The only difference in the elastic energy loss formalism occurs in eq. (35) (quoted here for convenience)

$$\frac{dN^c}{dx} = E\frac{d}{d\omega}\int dz\frac{dN^c}{dz} \tag{35}$$

Now dN^c/dz is explicitly dependent on z through its temperature dependence. Thus the approximation made in eq. (36) is no longer valid and we must do the z integral numerically.

4.3 Geometry Average

The details of this section will be very similar to that of section 2.1 and section 2.3, so we shall only highlight some of the changes that are needed in order to implement the fitted parameters approach

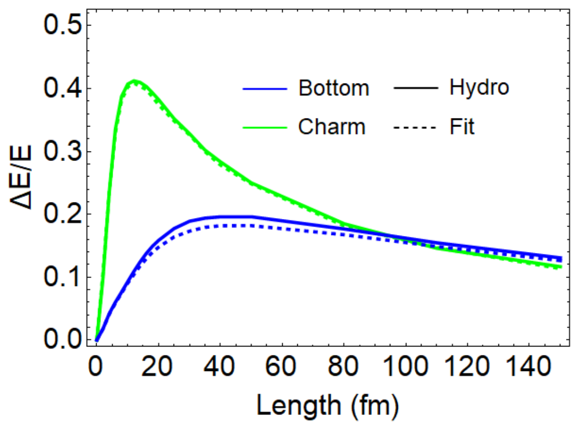

Figure 15: Comparison of energy loss for hydrodynamic temperature distribution and fitted temperature distribution for charm (mass = 1.2 GeV) and bottom (mass = 4.75 GeV) quarks. The temperature distribution (and thus like-wise the scattering centers) used in these results are the same as those used in fig. 14. Notice the good agreement between the fit and the hydrodynamic results. The energy loss curves for the charm and bottom quarks cross at high energy, this is because the distributions in eq. (42) and eq. (43) become peaked around $x = 0$ at high energy, as a result these regions become problematic to integrate over numerically. This is something that will need to be addressed in further work but with time constraints in mind, has been ignored here.

to calculating the average R_{AA}.

4.3.1 Averaging Over Every Path

As mentioned in section 4.1, $T(z) = T(z, z\cos(\phi) + x_0, z\sin(\phi) + y_0)$ with ϕ specifying the angle through the medium which the particular path is following and $\mathbf{x}_0 = (x_0, y_0)$ is the entry point into the medium. Using the modifications to the energy loss mentioned in section 4.2.1 we can calculate the average R_{AA} for each path, this is the *true average* of the R_{AA} discussed in section 2.1. The R_{AA} averaged over all the many paths is then (just as was the case in eq. (5))

$$\langle R_{AA}\rangle_t = \frac{\int d\phi d^2\mathbf{x}_0 \quad R_{AA}(\mathbf{x}_0, \phi) n_{coll}(\mathbf{x}_0)}{\int d\phi} \tag{54}$$

Calculating the average R_{AA} in this fashion will be computationally expense as we will need to calculate the energy loss for every path through the medium. However, calculating the R_{AA} this way will allow us to compare to the R_{AA} calculation using the fitted parameters approach (to be discussed next).

4.3.2 Averaging Over Fitted Parameters

The averaging process for the fitted parameters mimics that of the method described in section 2.4. For each ρ_0 and z_c, a probability is assigned to the likelihood of the parameter occurring. This assignment forms a probability distribution which we denote here as $P_{\rho z}$. The prescription we use for

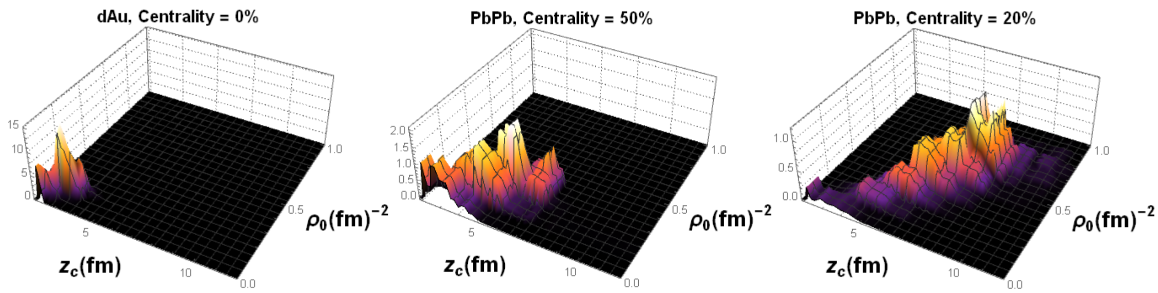

Figure 16: Probability distributions ($P_{\rho z}$) for the z_c and ρ_0 parameters. For *dAu* collisions we see the distribution is centered near small z_c and ρ_0 which indicates that small amounts of energy loss will occur. For *PbPb* collisions the distributions have most of their support in the regions where z_c and ρ_0 are large which suggests that more energy loss is to occur from these distributions

assigning these probabilities goes as follows:

1. For each path through the medium (which is specified by $\mathbf{x}_0$ and ϕ), we (numerically) find the critical length at which the thermalization occurs for the hydrodynamic temperature distribution $T(z)$. We then choose the ρ_0 parameter such that the condition in eq. (50) is satisfied. This means we have $z_c = z_c(\mathbf{x}_0, \phi)$ and likewise $\rho_0 = \rho_0(\mathbf{x}_0, \phi)$

2. For each direction ϕ and position $\mathbf{x}$, we weight the z_c and ρ_0 parameter by $n_{coll}(\mathbf{x})$ to obtain a spread of data of the form $n_{coll}(\mathbf{x})$ vs (z_c, ρ_0)

3. We then bin the $n_{coll}(\mathbf{x})$ vs (z_c, ρ_0) data and normalize it to obtain the $P_{\rho z}$ probability distribution for the fitted parameters (fig. 16)

The R_{AA} can be calculated as a function of the z_c and ρ_0 parameters by using the modified energy loss of section 4.2.1 along with the scattering centre eq. (49) and temperature distribution eq. (51) of section 4.1.1. The geometry average (using the fitted parameters) of the R_{AA} is then calculated as

$$\langle R_{AA} \rangle_g = \int d\rho_0 dz_c \quad R_{AA}(\rho_0, z_c) P_{\rho z}(\rho_0, z_c) \tag{55}$$

4.4 Results and Discussion

In this section we will present the results we get for the modified DGLV model using the fitted parameters approach to calculating an average R_{AA}.

In fig. 17 we compare the true average of the R_{AA} to the geometry average. We see that we get good agreement between the two calculations. It should be noted that we are working at first order in perturbation theory, so the level of disagreement between the models that is evident in fig. 17 is negligible.

It should be emphasized here, that calculating the geometry average is significantly less expensive computationally in comparison to the true average. But the different methods for calculating the average R_{AA} are in agreement with each other. This means we have found a method to calculate the R_{AA} that corresponds to a dynamic and realistic drop of QGP, and this method is computationally feasible.

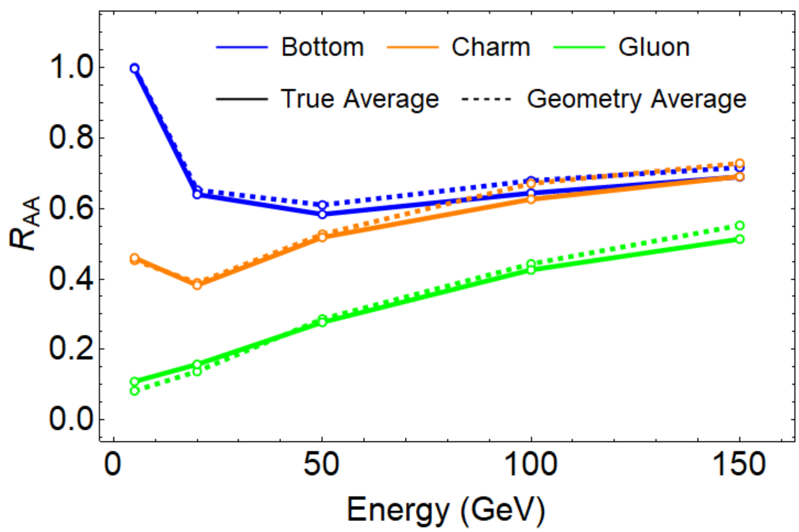

Figure 17: R_{AA} as a function on incoming parton energy for bottom quark, charm quark and gluons in *PbPb* collision at 20% centrality. Here we compare the predictions made by the true average and geometry average, we see good agreement between the two predictions in all three cases.

In fig. 18 we calculate the geometry average of the R_{AA} for a variety of collision systems, qualitatively our results give sensible predictions. The energy loss predicted is greater (which corresponds to a smaller R_{AA}) for lighter partons; we see more energy loss occurring in collision systems that have a greater centrality and less energy loss occurring in smaller collision systems.

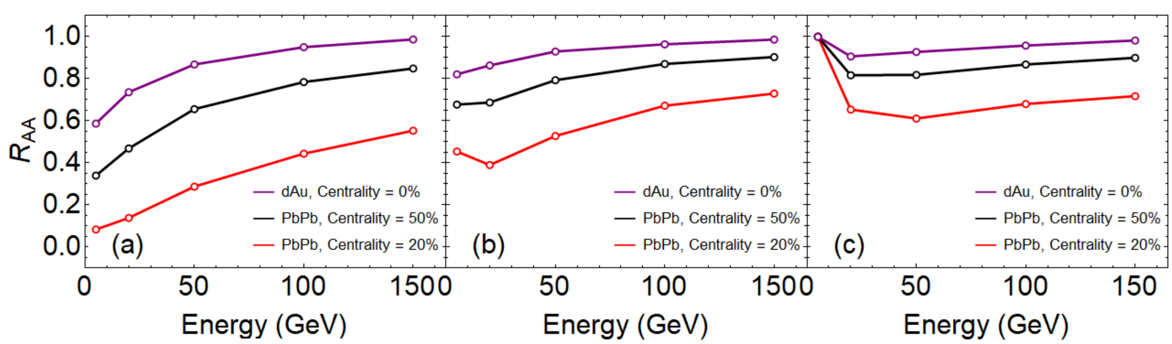

Figure 18: Geometry average results for gluons (a), charm quarks (b) and bottom quarks (c) for different collision systems. The $P_{\rho z}$ distributions for these collisions are shown in fig. 16

5

Conclusion and Outlook

The QGP is an exotic phase of matter that emerges as an extremely dense and hot plasma in high-energy collisions at research facilities such as the LHC and the RHIC. The plasma dominated the matter content of the early universe, and by studying the QGP, one can gain insights into the conditions that prevailed during these early moments in cosmic history.

This project has focused on understanding the energy loss of partons as they traverse the QGP. Specifically, we have examined an observable known as the R_{AA}, which is related to the suppression of high-energy partons due to their energy loss in the QGP medium.

In section 2, we described the R_{AA} observable and explored how it could be calculated theoretically. In order to make meaningful comparisons with experimental data, we argued that it is essential to calculate an average R_{AA} that accounts for the energy loss of numerous partons moving through the QGP. Two equivalent methods for calculating this average were considered. The first method, which we referred to as the *true average*, involves calculating the R_{AA} for every possible path that a parton could take through the QGP and averaging the results by weighting each individual path. However, this method proved to be computationally expensive and would not allow for comparison to experiment. The second method, referred to as the *geometry average*, involved calculating the R_{AA} as a function of effective lengths and temperatures. By obtaining a probability distribution P_{LT} for the effective lengths and temperatures, we could average the R_{AA} via this distribution. The geometry average method resulted in a significant computational advantage with an estimated speed up factor of order $\sim 10^7$, as the R_{AA} needed to be calculated far fewer times compared to the true average.

In section 3, we explored the DGLV energy loss model and its short path length correction in depth and demonstrated how the R_{AA} could be calculated from the model. This calculation explicitly assumed a simplified geometry of the QGP, where the medium was considered brick-like and stationary in time. Consequently, the R_{AA} could be expressed as a function of the length and temperature of the brick-like medium. However, as shown in fig. 12, this method of calculating the geometry average was sensitive to the effective length prescription and thus lacked robustness as the R_{AA} results spanned a wide range instead of converging to a uniform prediction.

To address this limitation, we introduced the *fitted parameters* approach for calculating the geometry average of the R_{AA} (section 4). This procedure allowed for a more accurate comparison between the true average and the geometry average (fig. 17). Our results demonstrated a good agreement between the two approaches. This good agreement means the model can describe the energy loss accurately while still being computationally feasible.

Future work on this project should include extending the current results to incorporate hadronization effects, which are essential for making comparisons with experimental data. Additionally, this project has focused primarily on the R_{AA} observable. While this is a significant observable to consider, future research should aim to describe other relevant quantities, such as the elliptic flow parameter v_2, to provide a more comprehensive understanding of the QGP. By incorporating these elements, we can improve the robustness and predictive power of the model, ultimately advancing our understanding of the QGP and its relevance to high-energy physics.

Phenomenological High Energy Physics is an ambitious field in the sense that it aims to describe some of the most extreme states of matter ever conceived. The complexity that comes along with the descriptions of these extreme states of matter is formidable. The only way for the field to progress is to find pockets of simplifications within the complexity and then exploit these to learn about the general properties of the matter in interest. The energy loss model presented in this work provides the field with a new tool to disentangle the complexity of the QGP and to describe the energy loss of partons moving through the medium.

Ultimately, this body of research has allowed us to take one step further in understanding the nuclear fireball known as the quark-gluon plasma which forms in the most technologically advanced experiments in all of science.

Appendix

A
The Glauber Model

The Glauber model provides a geometrical framework that captures the variety of the types of collisions one may expect in a particle accelerator. The model allows one to account for how directly head on a collision may be, and it does so in a very precise sense. Furthermore, the model can capture the effects that the different geometrical factors of colliding nuclei may have on final state observations.

A complete overview of the Glauber model can be found in [25]. Here I will briefly cover all the inputs from the Glauber model needed in our energy loss calculations.

Nuclear Charge Densities

We model the nuclear charge density (ρ) as a Fermi distribution which is known in the literature as a Wood-Saxon density distribution:

$$\rho(r) = \rho_0 \frac{1 + w(r/R)^2}{1 + \exp(\frac{r-R}{a})} \tag{56}$$

Where the parameters in the distribution represent:

- ρ_0 is the nucleon density at the center of the nucleus
- R is the radius of the nucleus
- a is the *skin depth*
- w parameterizes the deviation from spherical shape
- r is the distance from the center of the nucleus

Inelastic Nucleon-Nucleon Cross Section

Particle collisions at RHIC and the LHC involve multi-particle nucleon-nucleon processes, the cross sections of which are dominated by low-momentum transfers. This means that the nucleon-nucleon cross section (σ_{inel}^{NN}) cannot be calculated using perturbative techniques in QCD. However, the cross section can be determined experimentally and has been shown to vary from ~ 32 mb to ~ 42 mb. We will use $\sigma_{inel}^{NN} = 42$ mb for the sake of comaprison with previous work in all our calculations.

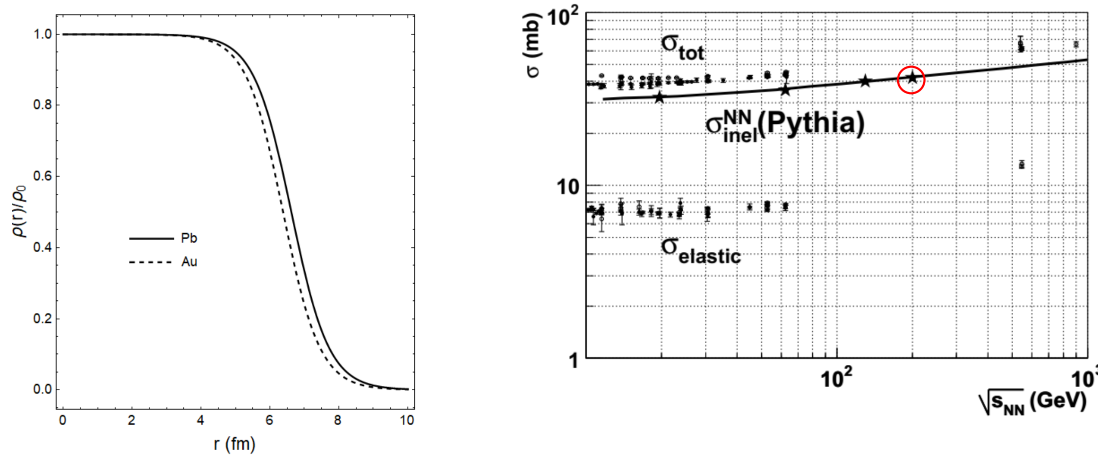

Figure 19: Left - Comparing the nucleon density of eq. (56) for gold (Au) and lead (Pb). Right - Inelastic nucleon-nucleon cross section σ_{inel}^{NN} as parameterized by Pythia [52, 53] (solid line) along with data on total and elastic nucleon-nucleon cross sections [54]. The star circled in red indicates the nucleon-nucleon cross section used for our energy loss calculations, namely $\sigma_{inel}^{NN} = 42\text{mb}$.

A.1 Interaction Probabilities

In order to derive the relevant geometric factors for a high energy nuclear collision, the Glauber model assumes that the trajectories of the nucleons within the nucleus are independent of each other. In order to derive these geometric factors, we consider fig. 20. Target A and projectile B are two heavy ions colliding at relativistic speeds, the number of nucleons in each of the heavy ions are also denoted by A and B. The impact parameter $\mathbf{b}$ is the distance between the centers of the two nuclei and is indicative of how central a collision is. The grey segments are used to represent two aligned flux tubes, which overlap during a collision. The tubes are at a displacement of $\mathbf{s}$ and $\mathbf{s} - \mathbf{b}$ from the center of A and B respectively. Since the nuclei are moving at near relativistic speeds, the spherical shape of the nuclei appear as Lorentz contracted *pancake* like disks with vanishing longitudinal widths from the perspective of the lab frame. To model the relativistic effect, we can integrate out the z dependency of the densities of the nuclei to obtain a flat pancake shaped nucleus. Hence the probability per unit transverse area of a nucleon being located in the target flux tube is:

$$\hat{T}_A(\mathbf{s}) = \int_0^\infty dz_A \hat{\rho}_A(\mathbf{s}, z_A) \tag{57}$$

where $\hat{\rho}_A(\mathbf{s}, z_A)$ is the probability per unit volume of finding a nucleon at location $(\mathbf{s}, z_A)$. We will use the Wood-Saxon distribution for $\hat{\rho}_A(\mathbf{s}, z_A)$. Similarly the expression for the probability per unit transverse area of a nucleon being located in the projectile flux tube is:

$$\hat{T}_B(\mathbf{s} - \mathbf{b}) = \int_0^\infty dz_B \hat{\rho}_B(\mathbf{s} - \mathbf{b}, z_B) \tag{58}$$

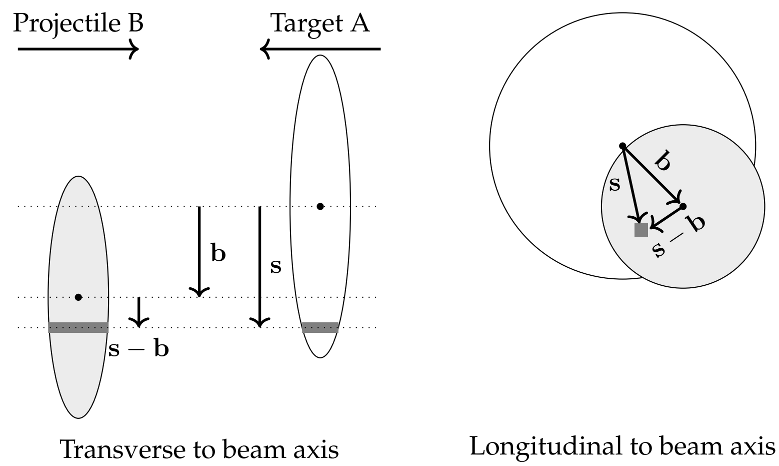

Figure 20: Schematic representation of a high energy collision from two viewpoints, namely transverse and longitudinal relative to the beam axis.

The product of $\hat{T}_A(\mathbf{s})\hat{T}_B(\mathbf{s}-\mathbf{b})d^2s$ would then give the probability per unit transverse area of the two nucleons being located in the flux tubes of A and B. From here we define a *thickness* function as:

$$\hat{T}_{AB}(\mathbf{b}) = \int \hat{T}_A(\mathbf{s}+\mathbf{b/2})\hat{T}_B(\mathbf{s}-\mathbf{b}/2)d^2s \tag{59}$$

We can interpret $\hat{T}_{AB}(\mathbf{b})$ as the area in which an interaction will occur between a specific nucleon in A and a given nucleon in B. For numerical reasons, we have implemented a coordinate shift of:

$$\mathbf{s} \to \mathbf{s}+\mathbf{b/2} \tag{60}$$

The probability of an interaction between a specific nucleon in A and a given nucleon in B is then:

$$P_{AB}(\mathbf{b}) = \hat{T}_{AB}(\mathbf{b})\sigma_{inel}^{NN} \tag{61}$$

In the Glauber model we only include the inelastic cross section as elastic [3] processes lead to very little energy loss and thus are ignored. Now the interaction between two nucleons is binary, that is they can either interact or not interact. We also suppose that the probability of interaction between any two pairs of nucleons in A and B should be given by eq. (61). This allows one to write the probability of n interactions occurring between the nucleus A and the nucleus B as a binomial distribution.

$$P(n,\mathbf{b}) = \frac{AB!}{n!(AB-n)!}[P_{AB}(\mathbf{b})]^n[1-P_{AB}(\mathbf{b})]^{AB-n} \tag{62}$$

[3] The elastic processes in the initial collision of the two nuclei can be ignored, but the elastic processes due to the interactions of the partons moving through the QGP certainly cannot be ignored

From eq. (62) we can find the total probability of an interaction occurring between the two nuclei as:

$$\frac{d^2\sigma_{inel}^{A+B}}{db^2} := p_{inel}^{A+B}(\mathbf{b}) = \sum_{n=1}^{AB} P(n,\mathbf{b}) = 1 - [1 - P_{AB}(\mathbf{b})]^{AB} \tag{63}$$

The notational suggestion used here, is to elucidate that the total probability of an interaction occurring is the differential cross section of the event.

If the nuclei are not polarized (which we assume is the case for all the nuclei we will investigate) then we can exploit the symmetry to obtain the total cross section (σ_{inel}^{A+B}). To do this, we first note that:

$$\mathbf{b} = (b_x, b_y) = (b\cos\theta, b\sin\theta) = (b\cos\theta', b\sin\theta') \tag{64}$$

where θ and θ' are any two polar angles. We then integrate the total probability of an interaction occurring to obtain σ_{inel}^{A+B}:

$$\begin{aligned}
\sigma_{inel}^{A+B} &= \int db^2 \quad \frac{d^2\sigma_{inel}^{A+B}}{db^2} && (65)\\
&= \int db^2 \quad \left(1 - [1 - P_{AB}(\mathbf{b})]^{AB}\right) && (66)\\
&= \int_0^{2\pi} d\theta \int_0^{\infty} db \quad b\left(1 - [1 - P_{AB}(b,\theta)]^{AB}\right) && (67)\\
&= \int_0^{\infty} db \quad 2\pi b\left(1 - [1 - P_{AB}(b)]^{AB}\right) && (68)
\end{aligned}$$

An important geometric quantity is that of N_{coll} which is the number of nucleon-nucleon collisions that occur when two nuclei collide. A nucleon of a one parent ion can collide at most once with every nucleon of the other parent ion. This implies that the maximum value N_{coll} can take on would be AB. We define N_{coll} as the average number of interactions occurring, hence:

$$N_{coll}(b) := \langle n \rangle = \sum_{n=1}^{AB} nP(n,b) = ABP_{AB}(b) \tag{69}$$

We can also define a density of number of collisions (n_{coll}) such that:

$$\begin{aligned}
N_{coll}(b) &= \int ds^2 n_{coll}(b) && (70)\\
\implies n_{coll}(b,s) &= \hat{T}_A(s + b/2)\hat{T}_B(s - b/2) && (71)
\end{aligned}$$

It should be noted that the number of hard processes between the constituents of the nucleons in a nucleus-nucleus collision scales like N_{coll}.

The final quantity of interest is the number of participants in a collision (N_{part}) which is thought of as the number of nucleons in the target and the projectile which undergo at least one collision. The number of participants is indicative of the centrality of the particular collision, for instance a larger number of participants would imply a more central collision.

This quantity is simply quoted from [25] as:

$$\begin{aligned} N_{part}(b) = A\int d^2s\hat{T}_A(s+b/2)[1-(1-\hat{T}_B(s-b/2)\sigma_{inel}^{NN})] \\ + B\int d^2s\hat{T}_B(s-b/2)[1-(1-\hat{T}_A(s+b/2)\sigma_{inel}^{NN})] \end{aligned} \tag{72}$$

The participant density ($n_{part}(b)$) is calculated in a manor similar to that of the density of collisions.

$$\begin{aligned} N_{part}(b) &= \int ds^2 n_{part}(b) \\ \implies n_{part}(b,s) &= A\hat{T}_A(s+b/2)[1-(1-\hat{T}_B(s-b/2)\sigma_{inel}^{NN})] \\ &+ B\hat{T}_B(s-b/2)[1-(1-\hat{T}_A(s+b/2)\sigma_{inel}^{NN})] \end{aligned} \tag{73}$$

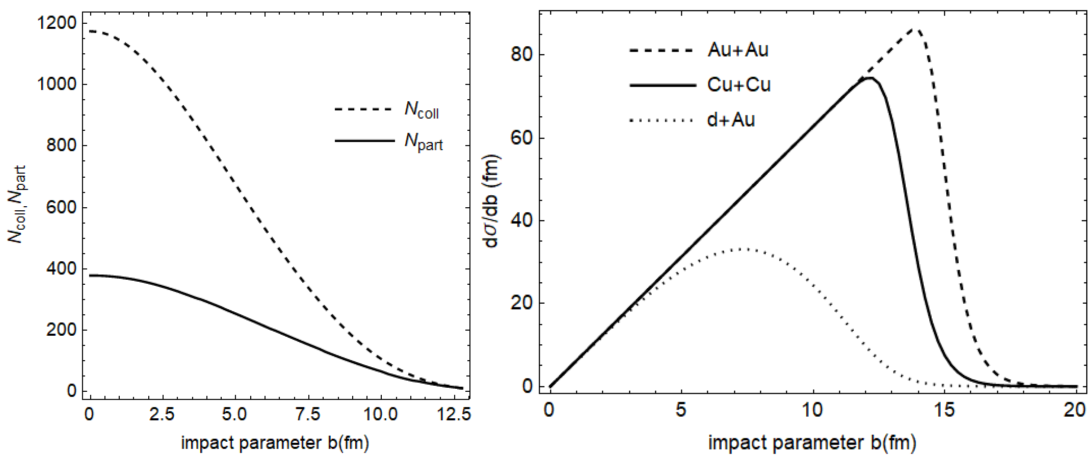

Figure 21: Left - Comparison of N_{coll} and N_{part} as functions of the impact parameter b. Right - Comparing the integrand of eq. (68) for gold-gold, copper-copper and deutron-gold collision types.

A.2 Temperature Dependence

Following [24], we can use the Glauber model to find a length (L) which is dependent on the temperature of the QGP (T). We have in general that the number of particles in a gas (N) is:

$$dN = gn_\epsilon d\tau = gn_\epsilon \frac{dVd^3\mathbf{p}}{(2\pi\hbar)^3} \tag{74}$$

- the occupation number is $n_\epsilon = 1/(exp[(\epsilon-\mu_c)/T] \pm 1)$ with - for bosons and + for fermions
- g is the degeneracy of states
- μ_c is the chemical potential

We assume the plasma to take the form of an ultrarelativistic gas in which each single-particle has energy $\epsilon = cp$. We further assume the plasma is isotropic, which then implies:

$$d^3\mathbf{p} = 4\pi p^2 dp = \frac{4\pi}{c^3}\epsilon^2 d\epsilon \tag{75}$$

From here we can obtain the number of fermions and bosons in the plasma. We take the chemical potential to be zero to obtain:

$$N_{B/F} = \frac{g}{(2\pi\hbar)^3}\int dV \int n_\epsilon d^3\mathbf{p} \tag{76}$$

$$= \frac{4\pi g V}{(2\pi\hbar c)^3}\int_0^\infty n_\epsilon \epsilon^2 d\epsilon \tag{77}$$

$$\implies \frac{N_B}{V} = \frac{g_B\zeta(3)}{\pi^2(\hbar c)^3}T^3 \quad \text{and} \quad \frac{N_F}{V} = \frac{3g_F\zeta(3)}{4\pi^2(\hbar c)^3} \tag{78}$$

The total number of particles in the plasma (N_{tot}) will just be the sum of the bosons (N_B) and fermions (N_F), hence:

$$\frac{N_{tot}}{V} = \frac{\zeta(3)}{\pi^2(\hbar c)^3}\left[g_B + \frac{3}{4}g_F\right]T^3 \tag{79}$$

$$\implies T = \left(\frac{\pi^2(\hbar c)^3}{\zeta(3)\left[g_B + \frac{3}{4}g_F\right]}\frac{N_{tot}}{V}\right)^{1/3} \tag{80}$$

From which we can obtain:

$$T = \left(\frac{\pi^2(\hbar c)^3}{1.202[2(n_c^2-1)+3n_c n_f]}\rho_D\right)^{1/3} \tag{81}$$

- n_f is the number of the number of active quark flavours, which is taken to be 2 throughout this manuscript as only the charm and bottom quark contribute to the observed spectra at the energy scales at which we are concerned
- n_c is the number of colour charges involved (namely, 3)
- $g_F = 2\cdot 2\cdot n_c \cdot n_f$ for spin $1/2$ quarks and anti-quarks
- $g_B = 2(n_c^2-1)$ for gluons in $SU(n_c)$ with two helicities
- $\zeta(3) \approx 1.202$ where ζ is the Riemann zeta function
- ρ_D is obtained from: $\rho_D = \frac{N_{tot}}{V}$

We then define ρ_D as:

$$\rho_D = \frac{2\beta}{L}\frac{\int d^2\mathbf{x} \quad (n_{part})^2}{\int d^2\mathbf{x} \quad n_{part}} \tag{82}$$

Where β is a smudge factor that is indicative of the centrality class and n_{part} (eq. (73)) is determined from the Glauber Model. In order to find β, we set the temperature in eq. (81) to 0.25GeV and

$L = 5$fm for our most central centrality class (0 to 5% centrality) and the solve for β. These choices are somewhat arbitrary, other combinations of temperature and lengths may be used and the effects of which have not been explored. We can then obtain our final result for the temperate as a function of length:

$$T = \left(\frac{2\beta}{L} \frac{\pi^2 (\hbar c)^3}{1.202[2(n_c^2 - 1) + 3n_c n_f]} \frac{\int d^2\mathbf{x} \quad (n_{part})^2}{\int d^2\mathbf{x} \quad n_{part}} \right)^{1/3} \tag{83}$$

Now, the Debye mass (μ) and the mean free path (λ) are themselves temperature dependent; we quote the results from [24].

$$\mu = T\sqrt{4\pi\alpha_s(1 + \frac{n_f}{6})} \tag{84}$$

$$\sigma_{gg} = \frac{9\pi\alpha_s^2}{2\mu^2} \quad \text{and} \quad \sigma_{qg} = \frac{4}{9}\sigma_{gg} \tag{85}$$

$$\rho_g = 16\frac{\zeta(3)}{\pi^2}T^3 \quad \text{and} \quad \rho_q = 9n_f\frac{\zeta(3)}{\pi^2}T^3 \tag{86}$$

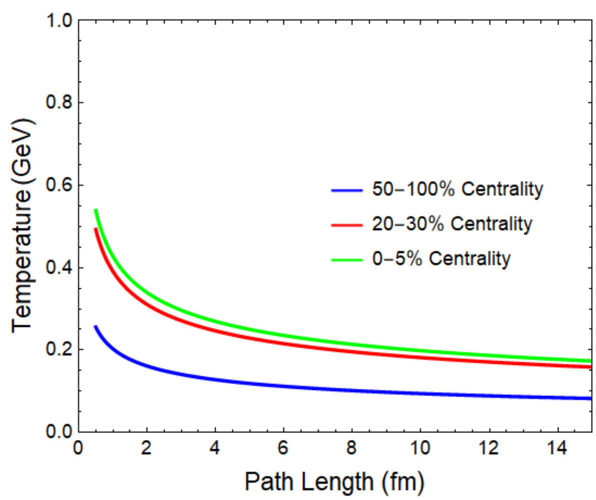

Figure 22: A comparison between the temperature profiles for different centrality classes as determined by eq. (83). For more central collisions we see that the temperature is higher which makes sense as the QGP is likely to have gained more energy from the incoming partons in a more direct collision. Using the prescription for the temperature outlined in this section, we found $\beta = 7.15$

$$\lambda = \frac{1}{\rho_g\sigma_{gg} + \rho_q\sigma_{gq}} \tag{87}$$

Here σ_{gg} and σ_{qg} are the cross sections for the gluon-gluon and quark-gluon interactions, while ρ_q and ρ_g are the densities of the quarks and gluons respectively

B

Details of the Energy Loss Calculation

B.1 Implementing the Radiative Energy Loss

The full form of eq. (22) can be computationally expensive, often one can simplify eq. (22) by assuming an explicit form for the scattering density $\bar{\rho}(\Delta z)$ and then doing the Δz integral analytically. If we assume that $\bar{\rho}(\Delta z)$ exponentially decays as

$$\bar{\rho}(\Delta z) = \frac{e^{-\Delta z/(L/2)}}{(L/2)} \tag{88}$$

Then one can arrive the following expression:

$$\begin{aligned} \frac{dE_{DGLV}}{dx} = \frac{2C_R\alpha_s LE}{\pi^2}\int d\mathbf{k}^2 \int d^2\mathbf{q} \quad & \frac{\left(\mu^2/\lambda\right)}{(\mathbf{k}^2+m_g^2+M^2x^2)(\mathbf{q}^2+\mu^2)^2} \\ \times & \frac{\mathbf{k}\cdot\mathbf{q}(\mathbf{k}-\mathbf{q})^2+(m_g^2+M^2x^2)\mathbf{q}\cdot(\mathbf{q}-\mathbf{k})}{(\frac{4Ex}{L})^2+\left((\mathbf{k}-\mathbf{q})^2+M^2x^2+m_g^2\right)^2} \end{aligned} \tag{89}$$

Where the $\mathbf{k}$ integral has been transformed as:

$$\int d^2\mathbf{k} \rightarrow \int_0^{2\pi} d\phi \int_0^{\infty} d|\mathbf{k}||\mathbf{k}| \rightarrow \pi \int_0^{\infty} d\mathbf{k}^2 \tag{90}$$

Equation (89) allows us to compare our model with previous work done in the field at large. Other forms for the scattering density have been explored in [27, 28].

The bounds for the integrals in eq. (89) are found by imposing kinematic restraints on the momenta — as was explored by [45]. Both $k = |\mathbf{k}|$ and $q = |\mathbf{q}|$ are bounded below by zero. The upper bound on k is derived from the three body kinematics (jet + gluon) to be $k_{max} = 2Ex(1-x)$. While q is bound from above by $q_{max} = \sqrt{3\mu E}$ in line with what was done in by [3, 55].

Now to implement eq. (89) numerically, we perform a coordinate transformation such that the angle between $\mathbf{k}$ and $\mathbf{q}$ is defined as the polar angle (θ). This allows us to write eq. (89) as[4]:

[4] The kernel of eq. (91) only has dependence on θ through $\cos(\theta)$, so to speed up the numerics, one can do the θ integral from 0 to π and then multiply the result by two.

$$\frac{dE_{DGLV}}{dx} = \frac{4C_R\alpha_s LE}{\pi^2\lambda}\int_0^{2\pi} d\theta \int_0^{q_{max}} dq \frac{q\mu^2}{(q^2+\mu^2)^2}\int_0^{k_{max}} dk \frac{k}{k^2+m_g^2+M^2x^2} \times \frac{(m_g^2+M^2x^2)(q^2-kq\cos\theta)+(kq\cos(\theta))(k^2-2kq\cos\theta+q^2)}{(k^2-2kq\cos\theta+q^2+m_g^2+M^2x^2)^2+\left(\frac{4Ex}{L}\right)^2} \tag{91}$$

The short path length correction part of eq. (22) reads as

$$\frac{dE_{SPLC}}{dx} = \frac{C_R\alpha_s LE}{\pi\lambda}\int \frac{d^2\mathbf{q}}{\pi}\frac{\mu^2}{(\mu^2+q^2)^2}\int\frac{d^2\mathbf{k}}{\pi}\int d\Delta z\bar{\rho}(\Delta z)\frac{e^{-\sqrt{\mu^2+q^2}\Delta z}}{2} \times \left\{\frac{\mathbf{k}^2}{\Delta^4}\left(1-\frac{2C_R}{C_A}\right)\left(1-\cos\left(\frac{\Delta^2}{xE}\Delta z\right)\right) + \frac{\mathbf{k}\cdot(\mathbf{k}-\mathbf{q})}{\Delta^2(\Delta^2+\mathbf{q}^2-2\mathbf{k}\cdot\mathbf{q})}\left[\cos\left(\frac{\Delta^2}{xE}\Delta z\right)-\cos\left(\frac{2\mathbf{k}\cdot\mathbf{q}-\mathbf{q}^2}{xE}\Delta z\right)\right]\right\} \tag{92}$$

where for notational convenience we have defined $\Delta^2 = k^2+m_g^2+M^2x^2$. Additionally, lets define another value $\Omega = 2+L\sqrt{\mu^2+q^2}$ as this will be useful in the next expression. We now again assume that the scattering centres take the form of eq. (88), we arrive at the following expression for the correction term.

$$\frac{dE_{SPLC}}{dx} = \frac{2C_R\alpha_s EL}{\pi^2}\int_0^{2\pi} d\theta\int_0^{k_{max}} dk\int_0^{q_{max}} dq\frac{kq(\mu^2/\lambda)}{(\mu^2+q^2)^2}\left\{\frac{k^2}{\Delta^4}\left(1-\frac{2C_R}{C_A}\right)\left(\frac{1}{\Omega}-\frac{\Omega}{\left(\frac{\Delta^2 L}{2xE}\right)^2+\Omega^2}\right) + \frac{\Omega(k^2-kq\cos\theta)}{\Delta^2(\Delta^2+q^2-2kq\cos\theta)}\left(\left[\left(\frac{\Delta^2 L}{2xE}\right)^2+\Omega^2\right]^{-1}-\left[\left(\frac{2kq\cos\theta-q^2}{2xE}\right)^2 L^2\right]^{-1}+\Omega^2\right)\right\} \tag{93}$$

The bounds for the integrals in eq. (93) are the same as those for eq. (89)

B.1.1 Effect of Short Path length Correction

The asymptotics of the DGLV with and without the short path length correction predict different behaviours in the energy loss of the parton. As shown by Kolbe and Horowitz [27], one finds that the energy loss of the uncorrected term (ΔE_{DGLV}) scales like:

$$\Delta E_{DGLV} = \frac{C_R\alpha_s}{4}\frac{L^2\mu^2}{\lambda}\log\left(\frac{E}{\mu}\right) \tag{94}$$

While the energy loss of the corrected term (ΔE_{SPLC}) in the large energy limit goes like:

$$\Delta E_{SPLC} = \frac{-C_R^2\alpha_s}{\pi C_A}\frac{L}{\lambda}\frac{1}{2+\mu L}E\log\left(\frac{2EL}{2+\mu L}\right) \tag{95}$$

So we see that eq. (94) and eq. (95) imply that the relative energy loss ($\Delta E_{SPLC}/\Delta E_{DGLV}$) grows as:

$$\frac{\Delta E_{SPLC}}{\Delta E_{DGLV}} \propto -E \tag{96}$$

In fig. 9 we see that the numerical results of the two models are in close agreement for low energies; the predictions begin to differ for higher energies as less energy loss occurs when the correction is included.

One should note that the energy loss can in fact be negative, this is apparent in the right panel of fig. 9. A negative energy loss arises as the calculations are all relative to the medium. So a gain in energy (negative energy loss) is just suggestive that the medium is suppressing radiation relative to what the vacuum would have suppressed.

Another interesting result to take note of, is that the mass contributions in eq. (89) and eq. (93) have a diminishing affect on the energy loss as the energy of the incoming parton is increased. This is evident in fig. 9 and fig. 10 as we see a convergence between the results for the bottom and charm quarks at high energies.

B.1.2 Screening Effects

In QED one encounters screening effects. This is a result of charged particles attracting oppositely charged particles and by Gauss' Law resulting in a effective charge that is dependent on the length scale at which the particle is being probed. The screening effect can be modeled through the Yukawa potential

$$V_{Yukawa} \propto \frac{e^{-\mu r}}{r} \tag{97}$$

Here μ^{-1} is the Debye length. For lengths $r << \mu^{-1}$ the potential mimics the form of the Coulomb potential with a $1/r$ dependency but as the length becomes comparable to the Debye length, the physics changes and the charged particle becomes screened.

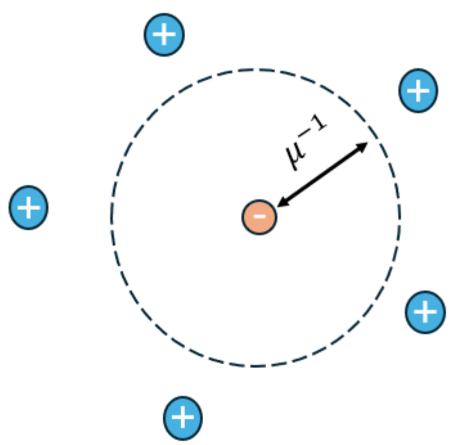

Figure 23: Illustration of screening. Positively charged particles then surround the negative charge and as such the system of both positive charges and the negative charge gain an effective charge. The potential of the effective charge is modeled through eq. (97), which introduces a mass parameter μ, this parameter can be seen as an effective mass.

In the case of QCD, the screening is very similar however the potential in eq. (97) is modified to have a random colour charge [43]. The screening effect can thus give the mass-less gluon an effective mass (m_g) which we (following [46]) take to be $m_g = \mu/\sqrt{2}$.

B.2 Multiple Emissions and Collisions

B.2.1 Convolutions of Distributions

At this point it will be useful to discuss what a *convolution* of two probability distributions is, as we will make use of this statistical technique throughout the remainder of the section. Convolutions arise in the situation where one is presented with two independent random variables X and Y and their corresponding probability distributions P_X and P_Y. Now, to find the distribution which corresponds the quantity $X + Y$ (denoted here as P_{X+Y}) one must perform the following operation [56]

$$P_{X+Y}(z) = P_X * P_y = \int dz' P_X(z')P_Y(z - z') \tag{98}$$

where the bounds of the integral in eq. (98) are such that the entire domains of P_X and P_Y have support.

B.2.2 Multiple Gluon Emissions

Here we shall derive the kernel for multiple gluon emissions. To begin, We define $p_1^{rad}(x)$ as the normalized single emission kernel:

$$p_1^{rad}(x) := \frac{1}{N^g}\frac{dN^g}{dx} \tag{99}$$

One can interpret $p_1^{rad}(x)$ as the probability of emitting a single gluon with a fraction x of the incoming partons energy. Naturally, we then define $p_0(x)^{rad}$, the probability of emitting no gluons, as:

$$p_0^{rad}(x) := \delta(x) \tag{100}$$

This is natural since the probability of fractional energy loss after no gluon emissions would be localised at zero. Now $p_2^{rad}(x)$, the fractional energy loss distribution of two emitted gluons, would be the sum of two single emission distributions. Under the assumption that the two single emissions are independent of each other, we can define $p_2^{rad}(x)$ as the convolution of two single emissions. Hence, we obtain:

$$p_2^{rad}(x) = \int dx_1 p_1^{rad}(x_1)p_1^{rad}(x - x_1) \tag{101}$$

Likewise, $p_3^{rad}(x)$ would be the convolution of the $p_2^{rad}(x)$ and $p_1^{rad}(x)$ distributions, and so forth. Continuing this procedure, we arrive at an expression for the fractional energy loss distribution for an arbitrary number (n) of gluon emissions

$$p_n^{rad}(x) = \int dx_{n-1} p_{n-1}^{rad}(x_{n-1})p_1^{rad}(x - x_{n-1}) \tag{102}$$

$$= \int \prod_{i=1}^{n-1} dx_i p_1(x_i) p_1\left(x - \sum_{j=1}^{n-1} x_j\right) \tag{103}$$

To then find the total probability of fractional energy loss for an incoming parton via gluon emission, $P_{rad}(x)$, we use results from elementary probability theory as follows:

$$P(A) = \sum_B P(A \cap B) \tag{104}$$

$$= \sum_B P(A|B)P(B) \tag{105}$$

Where B partitions the sample space, $P(A \cap B)$ is the probability that A and B occur while $P(A|B)$ is the conditional probability that A will occur given that B has occurred. From here we let $P(A) = P_{rad}(x)$ and $P(B) = p_n^{rad}(x)$. This means we can interpret $P(A|B)$ as the probability of fractional energy loss x occurring given that n gluons were emitted. Following the assumption that the number of gluon emissions is Poissonian, we are then able to associate $P(A|B)$ as the Poisson distribution for n number of emissions with an average of N^g emissions occurring, that is to say:

$$P(A|B) = \frac{(N^g)^n}{n!} e^{-N^g} \tag{106}$$

From here we can find an expression for the probability of radiative fractional energy loss:

$$P_{rad}(x) = \sum_{n=0}^{\infty} \frac{(N^g)^n}{n!} e^{-N^g} p_n^{rad}(x) \tag{107}$$

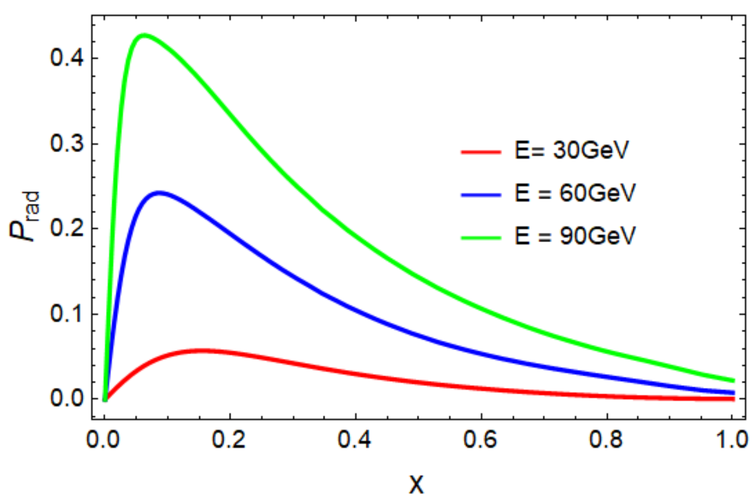

Figure 24: Equation (107) for charm quark at $T = 0.25$ GeV and various energies. Note that the delta distribution at $x = 0$ is not included in the plot.

B.2.3 Probability Leakage

Now, this scheme for calculating P_{rad} in eq. (107) may be mathematically sound. However, considering that x is the fraction of momentum lost of the incoming parton, we see that $p_1^{rad}(x)$ only has

has support for $x \in [0,1]$; now $p_2^{rad}(x)$ is obtained from

$$p_2^{rad}(x) = \int dx_1 \quad p_1^{rad}(x_1) p_1^{rad}(x - x_1) \tag{108}$$

the kernel of eq. (108) has support for $x_1 \in [0,1]$ and $(x - x_1) \in [0,1]$, which implies that $p_2^{rad}(x)$ has support for $x \in [0,2]$. In general, $p_n^{rad}(x)$ has support for $x \in [0,n]$. But x is the fraction of energy lost from the incoming parton, so x cannot be greater than 1 for our probability distributions to remain physical. The remedy to this mathematical issue, is to integrate $P_{rad}(x)$ from 0 to 1, and then place the rest of the weight of the distribution into a delta function centered at 1. This allows to redefine P_{rad} as

$$\tilde{P}_{rad} = P_{rad}(x) + W_{rad}\delta(x-1), \text{ with } x \in [0,1] \tag{109}$$

Where one obtains W_{rad} from

$$W_{rad} = \int_1^\infty dx P_{rad}(x) \tag{110}$$

The probability distribution of $W_{rad}\delta(x-1)$ can then be thought of the probability of a parton entering the QGP, then losing all of its energy due to radiation and ultimately coming to a halt. We can now write down our final result for the probability of fractional momentum loss due to radiation of multiple gluons:

$$\tilde{P}_{rad}(x) = \sum_{n=0}^{\infty} \frac{(N^g)^n}{n!} e^{-N^g} p_n^{rad}(x) + W_{rad}\delta(x-1) \tag{111}$$

It is worth noting that the infinite sum in eq. (107) cannot be implemented exactly in the numerics, so we evaluate the following ratio:

$$R(N) = \frac{\sum_{n=0}^{N} \int_0^1 dx \left[\frac{(N^g)^n}{n!} e^{-N^g} p_n^{rad}(x) \right]}{\int_0^1 dx \left[p_{N+1}^{rad}(x) \right]} \tag{112}$$

The series is then terminated once $R(N) < 10^{-3}$. This is only one method for terminating the series, others exist but yield similar results.

B.2.4 Multiple Collisions

In a very similar fashion to the derivation of eq. (42) one can obtain the probability for fractional momentum loss due to collisions occurring within the QGP ($\tilde{P}_{el}$). We state the final results here

$$p_0^{el}(x) = \delta(x) \tag{113}$$
$$p_1^{el}(x) = \frac{1}{N^c}\frac{dN^c}{dx} \tag{114}$$
$$p_n^{el}(x) = \int dx_{n-1} p_{n-1}^{el}(x_{n-1}) p_1^{el}(x - x_{n-1}) \tag{115}$$
$$P_{el}(x) = \sum_{n=0}^{\infty} \frac{(N^c)^n}{n!} e^{-N^c} p_n^{el}(x) \tag{116}$$
$$W_{el} = \int_1^{\infty} dx P_{el} \tag{117}$$
$$\tilde{P}_{el}(x) = P_{el}(x) + W_{el}\delta(x-1) \tag{118}$$

B.2.5 Total Energy Loss

We now have the probability distributions for the fractional energy loss of the incoming partons due to radiative energy loss ($\tilde{P}_{rad}(x)$) and collisional energy loss ($\tilde{P}_{el}(x)$). To obtain the total energy loss ($P_{tot}(x)$), we need to convolve $\tilde{P}_{rad}(x)$ and $\tilde{P}_{el}(x)$. Lets work out some of the details involved in this process

$$\begin{aligned} P_{tot}(x) &= \int dy \quad \tilde{P}_{el}(y)\tilde{P}_{rad}(x-y) \\ &= \int dy \quad [e^{-N^c}\delta(y) + P_{el}(y) + W_{el}\delta(y-1)] \\ &\times [e^{-N^g}\delta(x-y) + P_{rad}(x-y) + W_{rad}\delta(x-y-1)] \end{aligned} \tag{119}$$

using the following identity:

$$\int dx \quad \delta(x-a)\delta(x-b) = \delta(a-b) \tag{120}$$

we obtain

$$\begin{aligned} P_{tot}(x) &= e^{-(N^c+N^g)}\delta(x) + e^{-N^c}P_{rad}(x) + W_{rad}e^{-N^c}\delta(x-1) \\ &+ e^{-N^g}P_{el}(x) + \int dy P_{el}(y)P_{rad}(x-y) + W_{rad}P_{el}(x-1) \\ &+ W_{el}e^{-N^g}\delta(x-1) + W_{el}P_{rad}(x-1) + W_{el}W_{rad}\delta(x-2) \end{aligned} \tag{121}$$

When writing down eq. (119), the probability leakage that occurred in the radiative and elastic convolutional processes will again occur. So this leads us to define $\tilde{P}_{tot}$ as

$$\tilde{P}_{tot} = P_{tot} + W_{tot}\delta(x-1) \tag{122}$$

with W_{tot} defined as

$$W_{tot} = \int_1^{\infty} dx P_{tot}(x) \tag{123}$$

Note that in eq. (121), the $W_{el}W_{rad}\delta(x-2)$ term is actually absorbed into W_{tot} since P_{tot} only has support for $x \in (-\infty, 1]$

B.2.6 Energy Loss after Convolutions

In this little section I will show that the energy loss is does not change after convolutions. That is to say

$$\int dx \frac{dN}{dx} x = \frac{\Delta E}{E} = \int dx P_{rad}(x)$$

This is just a nice consistency check that our model is behaving correctly analytically. We begin by rewriting $P_{rad}(x)$ in a more convenient way. We also adopt the convenient notation $\frac{dN}{dx} = \partial N$.

$$\begin{aligned}
P_{rad}(x) &= \sum_{n=0}^{\infty} \frac{(N^g)^n}{n!} e^{-N^g} p_n(x) \\
&= e^{-N^g}\delta(x) + \sum_{n=1}^{\infty} \frac{(N^g)^n}{n!} e^{-N^g} p_n(x) \\
&= e^{-N^g}\delta(x) + \sum_{n=1}^{\infty} \frac{(N^g)^n}{n!} e^{-N^g} \int \prod_{i=1}^{n-1} dx_i p_1(x_i) p_1\left(x - \sum_{j=1}^{n-1} x_j\right) \\
&= e^{-N^g}\delta(x) + \sum_{n=1}^{\infty} \frac{e^{-N^g}}{n!} \int \prod_{i=1}^{n-1} dx_i \partial N(x_i) \quad \partial N\left(x - \sum_{j=1}^{n-1} x_j\right)
\end{aligned}$$

$$\implies \int dx \quad x P_{rad}(x) = \int dx \left[\sum_{n=1}^{\infty} \frac{e^{-N^g}}{n!} \int \prod_{i=1}^{n-1} dx_i \partial N(x_i) \quad \partial N\left(x - \sum_{j=1}^{n-1} x_j\right)\right] x$$

We now make a change of integration variable with $x \mapsto x' = x - \sum_{j=1}^{n-1} x_j$. This gives us:

$$\begin{aligned}
\int dx \quad x P_{rad}(x) &= \int dx' \left[\sum_{n=1}^{\infty} \frac{e^{-N^g}}{n!} \int \prod_{i=1}^{n-1} dx_i \partial N(x_i) \partial N(x')\right] \left[x' + \sum_{j=1}^{n-1} x_j\right] \\
&= \sum_{n=1}^{\infty} \frac{e^{-N^g}}{n!} \left[\int dx' \int \prod_{i=1}^{n-1} dx_i \partial N(x_i) \partial N(x')\right] \left[x' + \sum_{j=1}^{n-1} x_j\right] \\
&= \sum_{n=1}^{\infty} \frac{e^{-N^g}}{n!} \left[\int \prod_{i=1}^{n} dx_i \partial N(x_i)\right] \left[\sum_{j=1}^{n} x_j\right] \\
&= \sum_{n=1}^{\infty} \sum_{j=1}^{n} \frac{e^{-N^g}}{n!} \int \prod_{i=1}^{n} dx_i \partial N(x_i) x_j \\
&= \sum_{n=1}^{\infty} \sum_{j=1}^{n} \frac{e^{-N^g}}{n!} \left[\int dx_j \partial N(x_j) x_j\right] \left[\int \prod_{i \neq j} dx_i \partial N(x_i)\right]
\end{aligned}$$

Now we notice that two terms in the brackets separately evaluate to

$$\int dx_j \partial N(x_j) x_j = \frac{\Delta E}{E}$$
$$\int dx_i \partial N(x_i) = N^g$$

With this, we get the following

$$\begin{aligned}
\int dx \quad x P_{rad}(x) &= \sum_{n=1}^{\infty} \sum_{j=1}^{n} \frac{e^{-N^g}}{n!} \frac{\Delta E}{E} \left(N^g\right)^{n-1} \\
&= \sum_{n=1}^{\infty} \frac{e^{-N^g}}{(n-1)!} \frac{\Delta E}{E} \left(N^g\right)^{n-1} \\
&= \frac{\Delta E}{E} e^{-N^g} \sum_{n=1}^{\infty} \frac{\left(N^g\right)^{n-1}}{(n-1)!} \\
&= \frac{\Delta E}{E} e^{-N^g} e^{N_g}
\end{aligned}$$

Thus we get the desired result

$$\implies \int dx \quad x P_{rad}(x) = \frac{\Delta E}{E}$$

neat!

B.2.7 Probability Conservation

Here we will show that probability is conserved after convolutions. That is we will show that each p_n^{rad} term is individually normalized, and above that the entire Poisson convolution for P_{rad} is itself normalized. The p_1^{rad} term is trivial.

$$\begin{aligned}
N^g &= \int \frac{dN^g}{dx} \\
p_1^{rad}(x) &= \frac{1}{N^g} \frac{dN^g}{dx} \\
\int dx \quad p_1^{rad}(x) &= 1 \checkmark
\end{aligned}$$

For $n > 1$ we have

$$\begin{aligned}
p_n(x) &= \int dx_{n-1} p_{n-1}(x_{n-1}) p_1(x - x_{n-1}) \\
&= \int \prod_{i=1}^{n-1} dx_i p_1(x_i) p_1 \left(x - \sum_{j=1}^{n-1} x_j \right) \\
\int dx \quad p_n(x) &= \int dx \int \prod_{i=1}^{n-1} dx_i p_1(x_i) p_1 \left(x - \sum_{j=1}^{n-1} x_j \right) \\
&= \int dx' \int \prod_{i=1}^{n-1} dx_i p_1(x_i) p_1(x') \\
&= \int \prod_{i=1}^{n} dx_i p_1(x_i) \\
&= 1 \checkmark
\end{aligned}$$

And then lastly for P_{rad} we have

$$\begin{aligned}
P_{rad}(x) &= \sum_{n=0}^{\infty} \frac{(N^g)^n}{n!} e^{-N^g} p_n^{rad}(x) \\
\int dx P_{rad}(x) &= \sum_{n=0}^{\infty} \frac{(N^g)^n}{n!} e^{-N^g} \int dx p_n^{rad}(x) \\
&= \sum_{n=0}^{\infty} \frac{(N^g)^n}{n!} e^{-N^g} \\
&= e^{-N^g} e^{N^g} \\
&= 1 \checkmark
\end{aligned}$$

C

Minutia of the R_{AA}

C.1 Derivation of the Integral Form of the R_{AA}

Here we will derive the integral form of eq. (2). We consider the case of a parton losing fractional energy loss x during an event. The momentum of the final state (p_f) is then given by $p_f = (1-x)p_i$ where p_i is the initial state momentum. The number of partons observed in the final state is then.

$$dN(p_f) = dN(pi)P(x|p_i)dx \tag{124}$$

where $P(x|p_i)$ is the probability of fractional energy loss x occurring given an initial momentum p_i. We then have:

$$\frac{dN_{\text{final}}(p_f)}{dp_f} = \int dx \frac{dN_{\text{prod}}(p_i)}{dp_f} P(x|p_i) \tag{125}$$

$$= \int dx \frac{dN_{\text{prod}}(\frac{p_f}{1-x})}{dp_i} \left(\frac{1}{1-x}\right) P\left(x|\frac{p_f}{1-x}\right) \tag{126}$$

If we next assume that the production spectrum follows a power law of the form:

$$\frac{dN_{\text{prod}}(\frac{p_f}{1-x})}{dp_i} = \frac{A}{p_i^{n(p_i)}}$$

where A is some normalization constant, then we can further simplify the equation for the R_{AA} as:

$$R_{AA}(pT) = \frac{dN_{AA}/dp_T}{N_{coll}\; dN_{pp}/dp_T} \tag{127}$$

$$= \frac{N_{coll}\int dx \frac{dN_{\text{prod}}(\frac{p_T}{1-x})}{dp_i}\left(\frac{1}{1-x}\right) P\left(x|\frac{p_T}{1-x}\right)}{N_{coll}\frac{dN_{\text{prod}}(p_T)}{dp_T}} \tag{128}$$

$$= \frac{N_{coll}\int dx \frac{A}{p_i^{n(\frac{p_T}{1-x})}}\left(\frac{1}{1-x}\right) P\left(x|\frac{p_T}{1-x}\right)}{N_{coll}\frac{A}{p_T^{n(p_T)}}} \tag{129}$$

$$= \frac{N_{coll}\int dx \frac{A}{\left(\frac{p_T}{1-x}\right)^{n\left(\frac{p_T}{1-x}\right)}}\left(\frac{1}{1-x}\right) P\left(x|\frac{p_T}{1-x}\right)}{N_{coll}\frac{A}{p_i^{n(p_T)}}} \tag{130}$$

$$= \int dx P\left(x|\frac{p_T}{1-x}\right)(1-x)^{n\left(\frac{p_T}{1-x}\right)-1}\;\frac{p_T^{n(p_T)}}{p_T^{n\left(\frac{p_T}{1-x}\right)}} \tag{131}$$

If we now assume that $n(p_T)$ is a slowly varying, then we have

$$n(p_T/(1-x)) \approx n(p_T) \tag{132}$$

Furthermore, if we assume that P is approximately independent of p_T, so that

$$P\left(x|\frac{p_T}{1-x}\right) \approx P(x) \tag{133}$$

We can then arrive at an expression for the R_{AA}.

$$R_{AA} \approx \int dx P(x)(1-x)^{n(p_T)-1} \tag{134}$$

C.2 Equivalence of the True Average and Geometric Average

The formal prescription for P_{LT} was given in eq. (21). We restate it here for convenience

$$P_{LT}(L_{eff}, T_{eff}) = \frac{\sum_{\phi_i}\sum_{\mathbf{x}_i : L_{eff}(\mathbf{x}_i,\phi_i)=L_{eff}}\sum_{\mathbf{x}_i : T_{eff}(\mathbf{x}_i,\phi_i)=T_{eff}} n_{coll}(\mathbf{x}_i)}{\sum_{\phi_i}} \tag{135}$$

With this formal description of P_{LT}, we can show that the true average and the geometric average are actually equivalent. Note that in passing to the continuous limit, eq. (21) becomes:

$$P_{LT}(L,T) \mapsto \frac{\int d\phi d^2\mathbf{x} \quad \delta(L(\mathbf{x},\phi)-L)\delta(T(\mathbf{x},\phi)-T) \quad n_{coll}(\mathbf{x})}{\int d\phi} \tag{136}$$

With $P_{LT}(L,T)$ now defined in the continuous limit, we can calculate the average R_{AA} explicitly

$$\begin{aligned}
\langle R_{AA}\rangle_g &= \int dLdT \quad R_{AA}(L,T)P_{LT}(L,T) \\
&= \left(\int d\phi\right)^{-1} \int dLdTd\phi d^2\mathbf{x} \quad \{\, R_{AA}(L(\mathbf{x},\phi),T(\mathbf{x},\phi))n_{coll}(\mathbf{x}) \\
&\qquad\qquad\qquad\qquad\qquad \times\delta(L(\mathbf{x},\phi)-L)\delta(T(\mathbf{x},\phi)-T)\ \} \\
&= \frac{\int d\phi d^2\mathbf{x} \quad R_{AA}(\mathbf{x},\phi)n_{coll}(\mathbf{x})}{\int d\phi} \\
&= \langle R_{AA}\rangle_t
\end{aligned}$$

which is precisely what we wrote down in eq. (5).

C.3 Explicit form of the R_{AA}

Equation (122) is the probability distribution we will use in calculating the R_{AA} eq. (2). Explicitly this will take the following form

$$\begin{aligned}
R_{AA} &= \int_{-\infty}^{1} dxP_{tot}(x)(1-x)^{n(p_T)-1} \\
&= e^{-(N^c+N^g)} + e^{-N^c}\int_{-\infty}^{1} dxP_{rad}(x)(1-x)^{n(p_T)-1} \\
&+ e^{-N^g}\int_{-\infty}^{1} dxP_{el}(x)(1-x)^{n(p_T)-1} + \int_{-\infty}^{1} dx\int_{-\infty}^{1} dyP_{el}(y)P_{rad}(x-y)(1-x)^{n(p_T)-1} \\
&+ W_{rad}\int_{-\infty}^{1} dxP_{el}(x-1)(1-x)^{n(p_T)-1}
\end{aligned} \tag{137}$$

Which leaves us with five nonzero terms. All deltas at 1 or beyond gave a vanishing contribution to the R_{AA}, while the $P_{rad}(x-1)$ term with a shifted argument also vanished as it had no support on the interval $x \in (-\infty, 1]$.

References

[1] M. van Leeuwen. Comparing energy loss phenomenology. *PoS*, High-pT physics09:002, 2009.

[2] Nestor Armesto, Brian Cole, Charles Gale, William A. Horowitz, Peter Jacobs, Sangyong Jeon, Marco van Leeuwen, Abhijit Majumder, Berndt Müller, Guang-You Qin, Carlos A. Salgado, Björn Schenke, Marta Verweij, Xin-Nian Wang, and Urs Achim Wiedemann. Comparison of jet quenching formalisms for a quark-gluon plasma "brick". *Phys. Rev. C*, 86:064904, Dec 2012.

[3] Magdalena Djordjevic and Miklos Gyulassy. Heavy quark radiative energy loss in qcd matter. *Nuclear Physics A*, 733(3):265–298, 2004.

[4] E. Rutherford. The scattering of alpha and beta particles by matter and the structure of the atom. *Phil. Mag. Ser. 6*, 21:669–688, 1911.

[5] Hideki Yukawa. On the Interaction of Elementary Particles I. *Proc. Phys. Math. Soc. Jap.*, 17:48–57, 1935.

[6] Steven Weinberg. The search for unity: Notes for a history of quantum field theory. *Daedalus*, 106(4):17–35, 1977.

[7] S. H. Neddermeyer and C. D. Anderson. Note on the Nature of Cosmic Ray Particles. *Phys. Rev.*, 51:884–886, 1937.

[8] M Gell-Mann. The eightfold way: A theory of strong interaction symmetry. *OSTI.GOV*, 3 1961.

[9] Y. Ne'eman. Derivation of strong interactions from a gauge invariance. *Nuclear Physics*, 26(2):222–229, 1961.

[10] Murray Gell-Mann. A Schematic Model of Baryons and Mesons. *Phys. Lett.*, 8:214–215, 1964.

[11] G. Zweig. An SU(3) model for strong interaction symmetry and its breaking. Version 2. *Developments in the Quark Theory of Hadrons*, pages 22–101, 2 1964.

[12] Akhilesh Ranjan and V Ravishankar. Introduction to quark-gluon plasma. *Indian Journal of Physics*, 84:11–40, 01 2010.

[13] David J. Gross and Frank Wilczek. Ultraviolet Behavior of Nonabelian Gauge Theories. *Phys. Rev. Lett.*, 30:1343–1346, 1973.

[14] H. David Politzer. Reliable Perturbative Results for Strong Interactions? *Phys. Rev. Lett.*, 30:1346–1349, 1973.

[15] Vardan Khachatryan et al. Measurement and QCD analysis of double-differential inclusive jet cross sections in pp collisions at $\sqrt{s} = 8$ TeV and cross section ratios to 2.76 and 7 TeV. *JHEP*, 03:156, 2017.

[16] Tapan Nayak. Quark-gluon plasma: Present and future. *arXiv*, 05 2008.

[17] Jean Letessier and Johann Rafelski. *Hadrons and Quark–Gluon Plasma*. Cambridge Monographs on Particle Physics, Nuclear Physics and Cosmology. Cambridge University Press, 2002.

[18] Urs Achim Wiedemann. Introductory Overview of Quark Matter 2012. *Nucl. Phys. A*, 904-905:3c–10c, 2013.

[19] Tadaaki Isobe. Measurements of high-pt neutral mesons in s[sub nn] = 200 gev au+au and cu+cu collisions at rhic-phenix. *AIP conference proceedings*, 01 2006.

[20] John Lajoie. Jets and parton energy loss at rhic: experimental status. *Brazilian Journal of Physics*, 37:825–829, 06 2007.

[21] A. Bazavov, Tanmoy Bhattacharya, C. DeTar, H.-T. Ding, Steven Gottlieb, Rajan Gupta, P. Hegde, U. M. Heller, F. Karsch, E. Laermann, L. Levkova, Swagato Mukherjee, P. Petreczky, C. Schmidt, C. Schroeder, R. A. Soltz, W. Soeldner, R. Sugar, M. Wagner, and P. Vranas. Equation of state in $(2+1)$-flavor qcd. *Phys. Rev. D*, 90:094503, Nov 2014.

[22] Shreyasi Acharya et al. The ALICE experiment: a journey through QCD. *Eur. Phys. J. C*, 84(8):813, 2024.

[23] Miklos Gyulassy and Michael Plümer. Jet quenching as a probe of dense matter. *Nuclear Physics A*, 527:641–644, 1991.

[24] William A. Horowitz. Probing the Frontiers of QCD. Other thesis, Columbia University, 11 2010.

[25] Michael L. Miller, Klaus Reygers, Stephen J. Sanders, and Peter Steinberg. Glauber modeling in high energy nuclear collisions. *Ann. Rev. Nucl. Part. Sci.*, 57:205–243, 2007.

[26] Coleridge Faraday, Antonia Grindrod, and W. A. Horowitz. Inconsistencies in, and short path-length correction to, $R_{AA}(p_T)$ in $\mathrm{A}+\mathrm{A}$ and $\mathrm{p}+\mathrm{A}$ collisions. *Eur. Phys. J. C*, 83(11):1060, 2023.

[27] Isobel Kolbe and W. A. Horowitz. Short path length corrections to Djordjevic-Gyulassy-Levai-Vitev energy loss. *Phys. Rev. C*, 100(2):024913, 2019.

[28] Isobel Kolbe and W. A. Horowitz. Short path length pQCD corrections to energy loss in the quark gluon plasma. *J. Phys. Conf. Ser.*, 802(1):012006, 2017.

[29] Simon Wicks, William Horowitz, Magdalena Djordjevic, and Miklos Gyulassy. Elastic, inelastic, and path length fluctuations in jet tomography. *Nucl. Phys. A*, 784:426–442, 2007.

[30] Beat Hahn, D. G. Ravenhall, and Robert Hofstadter. High-Energy Electron Scattering and the Charge Distributions of Selected Nuclei. *Phys. Rev.*, 101:1131–1142, 1956.

[31] Bjoern Schenke, Chun Shen, and Prithwish Tribedy. Running the gamut of high energy nuclear collisions. *Phys. Rev. C*, 102(4):044905, 2020.

[32] Bjoern Schenke, Prithwish Tribedy, and Raju Venugopalan. Event-by-event gluon multiplicity, energy density, and eccentricities in ultrarelativistic heavy-ion collisions. *Phys. Rev. C*, 86:034908, 2012.

[33] Bjoern Schenke, Prithwish Tribedy, and Raju Venugopalan. Fluctuating Glasma initial conditions and flow in heavy ion collisions. *Phys. Rev. Lett.*, 108:252301, 2012.

[34] Bjorn Schenke, Sangyong Jeon, and Charles Gale. Elliptic and triangular flow in event-by-event (3+1)D viscous hydrodynamics. *Phys. Rev. Lett.*, 106:042301, 2011.

[35] Bjorn Schenke, Sangyong Jeon, and Charles Gale. Higher flow harmonics from (3+1)D event-by-event viscous hydrodynamics. *Phys. Rev. C*, 85:024901, 2012.

[36] Bjoern Schenke, Sangyong Jeon, and Charles Gale. (3+1)D hydrodynamic simulation of relativistic heavy-ion collisions. *Phys. Rev. C*, 82:014903, 2010.

[37] S. A. Bass et al. Microscopic models for ultrarelativistic heavy ion collisions. *Prog. Part. Nucl. Phys.*, 41:255–369, 1998.

[38] M. Bleicher et al. Relativistic hadron hadron collisions in the ultrarelativistic quantum molecular dynamics model. *J. Phys. G*, 25:1859–1896, 1999.

[39] M. Gyulassy, P. Levai, and I. Vitev. Jet tomography of Au+Au reactions including multigluon fluctuations. *Phys. Lett. B*, 538:282–288, 2002.

[40] Urs Achim Wiedemann. Jet quenching versus jet enhancement: A Quantitative study of the BDMPS-Z gluon radiation spectrum. *Nucl. Phys. A*, 690:731–751, 2001.

[41] Yuan-Yuan Zhang, Guang-You Qin, and Xin-Nian Wang. Parton Energy Loss in Generalized High Twist Approach. *PoS*, HardProbes2018:102, 2018.

[42] Peter Brockway Arnold, Guy D Moore, and Laurence G. Yaffe. Transport coefficients in high temperature gauge theories. 2. Beyond leading log. *JHEP*, 05:051, 2003.

[43] Miklos Gyulassy, Peter Levai, and Ivan Vitev. Jet quenching in thin quark gluon plasmas. 1. Formalism. *Nucl. Phys. B*, 571:197–233, 2000.

[44] Isobel Kolbe. Short path length pQCD corrections to energy loss in the quark gluon plasma. Master's thesis, Cape Town U., 2015.

[45] M. Gyulassy, P. Levai, and I. Vitev. Reaction operator approach to nonAbelian energy loss. *Nucl. Phys. B*, 594:371–419, 2001.

[46] Magdalena Djordjevic and Miklos Gyulassy. The Ter-Mikayelian effect on QCD radiative energy loss. *Phys. Rev. C*, 68:034914, 2003.

[47] Miklos Gyulassy and Xin-nian Wang. Multiple collisions and induced gluon Bremsstrahlung in QCD. *Nucl. Phys. B*, 420:583–614, 1994.

[48] Eric Braaten and Markus H. Thoma. Energy loss of a heavy quark in the quark - gluon plasma. *Phys. Rev. D*, 44(9):R2625, 1991.

[49] Simon Wicks. Fluctuations with small numbers: Developing the perturbative paradigm for jet physics in the QGP at RHIC and LHC. Other thesis, Columbia University, 2008.

[50] Michael E. Peskin and Daniel V. Schroeder. *An Introduction to quantum field theory*. Addison-Wesley, Reading, USA, 1995.

[51] Coleridge Faraday and W. A. Horowitz. Collisional and Radiative Energy Loss in Small Systems. *arXiv*, 8 2024.

[52] J.P. Guillaud and A.E. Sobol. Simulation of diffractive and non-diffractive processes at the LHC energy with the PYTHIA and PHOJET MC event generators. Technical report, NA, 2004.

[53] Torbjorn Sjostrand, Stephen Mrenna, and Peter Z. Skands. PYTHIA 6.4 Physics and Manual. *JHEP*, 05:026, 2006.

[54] R. Michael Barnett et al. Review of particle physics. Particle Data Group. *Phys. Rev. D*, 54(1):1–720, 1996.

[55] Hannah Clayton, Matthew D. Sievert, and W. A. Horowitz. Jet broadening in the opacity and twist expansions. *Eur. Phys. J. C*, 82(5):437, 2022.

[56] Mehran Kardar. *Statistical Physics of Particles*. Cambridge University Press, 2007.